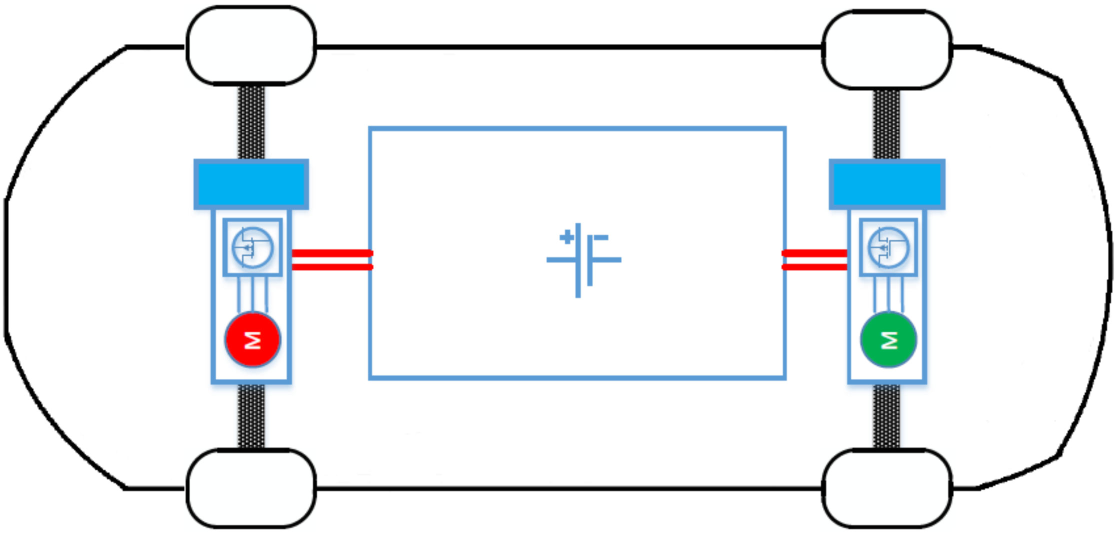

Scalable Integrated Drive System

for Battery Electric Vehicles

Master's thesis in Electric Power Engineering

Nimananda Sharma

Department of Energy and Environment
CHALMERS UNIVERSITY OF TECHNOLOGY
Gothenburg, Sweden 2017

Master's thesis 2017:NN

Scalable Integrated Drive System

for Battery Electric Vehicles

Nimananda Sharma

Department of Energy and Environment
Division of Electric Power Engineering
Chalmers University of Technology
Gothenburg, Sweden 2017

Scalable Integrated Drive System
for Battery Electric Vehicles
Nimananda Sharma

© Nimananda Sharma, 2017.

Supervisor: Yujing Liu, Electric Power Engineering
Examiner: Yujing Liu, Electric Power Engineering

Master's Thesis 2017:NN
Department of Energy and Environment
Division of Electric Power Engineering
Chalmers University of Technology
SE-412 96 Gothenburg
Telephone +46 31 772 1000

Cover: A scalable integrated drive system architecture using two drive units.

Scalable Integrated Drive System
for Battery Electric Vehicles
Nimananda Sharma Department of Energy and Environment
Chalmers University of Technology

Abstract

Conventionally, electric powertrain in battery electric vehicles are designed and optimized for a particular vehicle category and performance requirements. In this thesis the design of an electric powertrain using two different type of machine is proposed which can be implemented across passenger vehicle categories and provide various performance levels. One of the machine will be high efficiency and the other capable of providing high peak power. The powertrain is dimensioned by analysing existing combustion engine based as well as battery electric vehicle specifications along with wheel load analysis performed on simplified vehicle models using standard drive cycles. Two different vehicle models representing a small and medium sized car is used. The acceleration requirements of various drive cycles are observed to mainly determine the peak power of the powertrain. A V-shaped interior permanent magnet machine is designed to support most of the drive cycle requirements with an electromagnetically excited synchronous machine to provide overloading capabilities. To compare the proposed drive system with the two different machines, a third machine using the same V-shaped magnet geometry is designed to represent a conventional electric powertrain. The proposed drive system is observed to achieve similar torque speed operating boundary as the centralized drive using single machine. The peak efficiency of the centralized drive motor was observed to be higher and the efficiency contours were wider as expected. However, the average operating efficiency of the centralized drive machine was found to be inferior to the proposed design. It was observed that the proposed design of the powertrain can result in higher operating efficiency while providing a scalablity of peak power.

Keywords: distributed drive, integrated drive, scalable drive, battery electric vehicle, drive cycle, wheel power analysis, PMSM, EESM, high efficiency motor, vehicle model.

Acknowledgements

I would first like to express my sincere gratitude to my supervisor and examiner Professor Yujing Liu for the many discussions and his feedback that helped shape the idea for this master thesis. His guidance and support during the whole thesis work was fundamental to the completion of the work. Also, I would like to thank Junfei Tang for letting me use his MATLAB code for generating the efficiency map and for spending his valuable time to help me with the design of the machines.

I am thankful to my family for supporting me emotionally and financially throughout my study and for letting me pursue my interests.

I want to thank Dr. Pär Ingelström from Volvo AB and Jonas Forssell from Volvo Cars for their valuable feedbacks. I would always be thankful to Chalmers for providing me the opportunity to study and supporting me with scholarhips.

Nimananda Sharmna, Gothenburg, May 2017

Contents

List of Figures

List of Tables

1

Introduction

Electric vehicles started to re-gain popularity in the beginning of the 21st century. This can be mostly attributed to the two significant events. First, the worldwide launch of Toyota Prius Hybrid, world's first mass produced hybrid electric vehicle in 2000. Second, the announcement made by Tesla, a Silicon Valley start up to produce a luxury electric vehicle capable of driving more than 300 km on a single charge. The success of Tesla led to other automotive manufacturers launching their own electric vehicle e.g. Nissan Leaf, Chevy Bolt etc.[1]. However, the powertrain configurations of most electric vehicles have so far remained the same as conventional internal combustion engines with a single engine and transmission system [2]. This may be caused by the fact that, most hybrid and electric vehicles available today in the market are conversions or modifications of existing vehicles running on internal combustion engine [3].

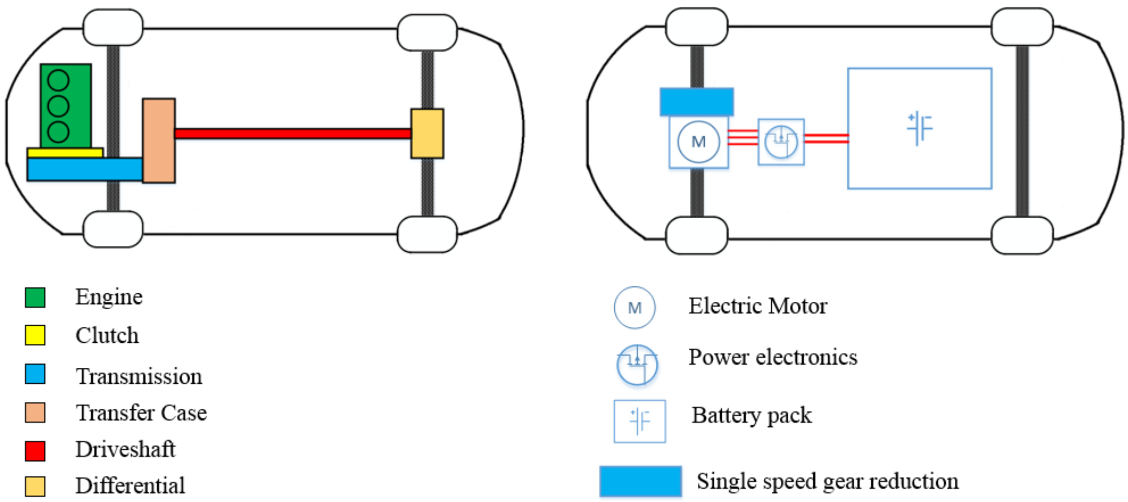

Figure 1.1: The centralized drive configuration derived from internal combustion engine based vehicles

The powertrain topology of current battery electric vehicle (BEVs) can be described as a centralized drive comprising of a single motor, power electronics and a high voltage battery pack as shown in figure 1.1 e.g Nissan Leaf, [4]. As shown in figure 1.1, this topology is derived from powertrains based on internal combustion engine [5]. The powertrains designed based on this configuration are usually optimized for performance to suit a particular vehicle model. Considering the limited number of

BEV models available today and there peak power specification, this powertrain topology can be considered to be optimal [6]. However, as the electric motor and power electronics dimension increases yielding higher peak power, it may be difficult to implement such topologies without significantly changing the vehicle design. In such cases, it may be beneficial to use multiple drive units. An example is the Tesla Model S dual motor configuration where a high performance motor is used on the rear shaft along with another motor on the front shaft [7]. This type of drive train topology as shown in figure 1.2 can be referred to as distributed drive.

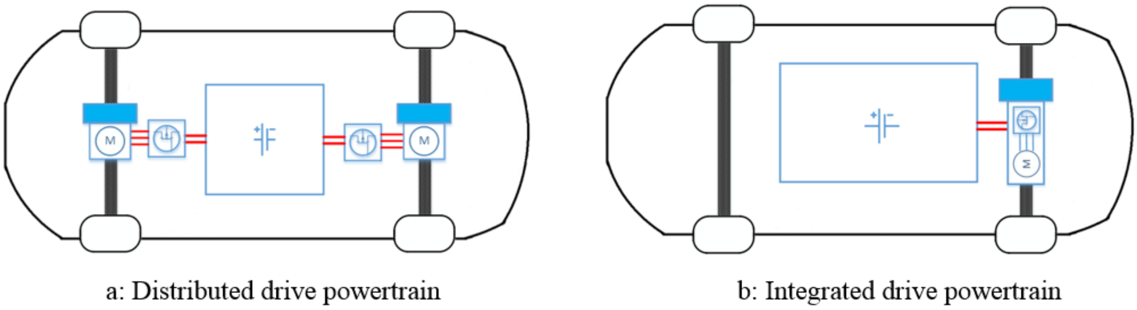

Figure 1.2: Schematics of distributed and integrated powertrain configurations

According to [4], distributed drive topology can use in-wheel motor or/and wheel-side motors to drive the wheels. The in-wheel motor designed concept have been demonstrated in the past and documented in literature [9]-[14]. The in-wheel motor design is usually direct driven without gear reduction which can result in higher efficiency. Also, the wheel housing is used as motor housing. However, it suffers from the problem of increased un-sprung mass which can negatively impact the vehicle ride and handling performance. These motors also have low power and torque densities as a motor without speed reducing gear must produce very high torque in low speed region to support vehicle starting [4]. So, in this study the focus will be towards wheel-side motor configuration. As the size of both motor and power electronics can be reduced using distributed drive topology, it may be possible to integrate the motor and power electronics in one unit. In figure 1.2, an integrated drive configuration using a single drive unit is shown.

The battery electric vehicles available today provide a fixed performance which may vary among vehicle manufacturers in terms of maximum power and torque [6]. Unlike, internal combustion engine based vehicles (ICEVs) there are no powertrain choices available to the customer or scalability in terms of maximum power for the same vehicle model. It may be due to the limited number of BEVs available in the market compared to ICEVs. But, judging by the increase in EV sale, it is safe to assume that the number of BEV models will be significantly higher in a decade or so [6]. In the case of ICEVs, the peak power can be increased by using turbochargers, superchargers etc. However, the peak power of an electric motor is limited by design e.g. size, thermal loading, converter rating etc. So, scalability in power can't be achieved in the same way as possible with combustion engine. So, in this project a scalable electric powertrain design is considered using combination of multiple drive units similar to distributed drive. The individual drive units are expected to have low power ratings creating the possibility of integrating the motor and power electronics. The individual drive units can be identical as in the case of Tesla Model S [7] and Mercedes SLS AMG [8] or constitute of two different type drive units as shown in figure 1.3.

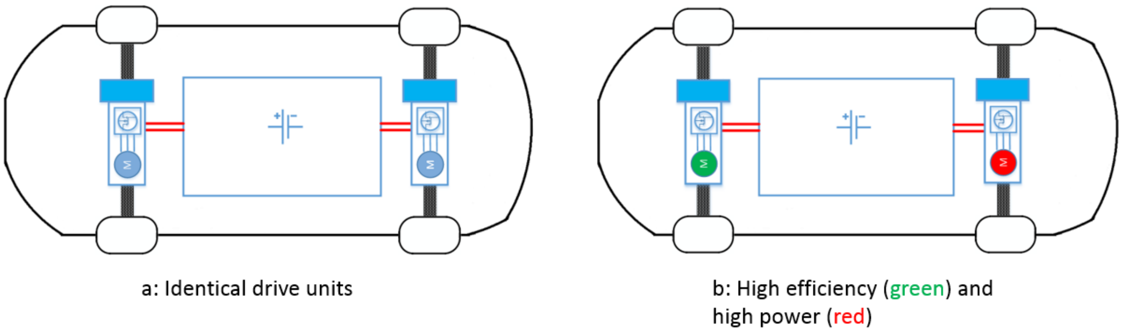

Figure 1.3: Two possible design of scalable electric powertrain for BEVs

In this project, the second configuration with two different type of drive units will be considered. The two type of drive units considered as shown in figure 1.3b are classified as high efficiency and high power drive. The high efficiency drive will use a Permanent Magnet Synchronous machine (PMSM) and will be optimized for efficiency. The high power drive as the name suggest will be designed for having high peak power. Electrical excited synchronous machine (EESM) will be used. The peak power of such a powertrain can be scaled up easily by adding multiple units to achieve desired acceleration performance in the vehicle. The proposed main advantage of this drive system are outline as below

- As the powertrain is scalable, apart from being able to achieve different acceleration performance by simply using multiple units as suggested above, the powertrain itself can be designed to be independent of vehicle category e.g. small, medium, large etc [6]. Hence, there is a possiblity of standardizing the powertrain across vehicle models and achieve economy of scale.
- The drive system uses two different drive units. So, it offers more design freedom e.g. the high efficiency drive can be designed to supply drive cycle power demanded by the vehicle and peak power for the desired acceleration performance can be supplied via the high power motor.
- The advantages of independent wheel drive can be realized in case of the fully scaled powertrain using 4 drive units e.g. traction control, anti-lock braking system etc can be implemented in the motor control without additional hardware.
- Integrating the machine and power electronics in the same housing, the cooling can be shared. Also, the need for cables between power electronics and machine can be eliminated.

1.1 Aim

The aim of this work is to propose the design of future electric power train using a drive cycle optimized high efficiency machine couple with another motor having high overloading capacity to fulfill the acceleration requirements. Two different motors are designed initially and the performance of the proposed design with two motor is compared with a third machine designed to represent conventional powertrain design to evaluate the suitability.

1.2 Method

To understand the various electric drive train topologies and previous work, a literature survey was conducted mainly using online resources such as technical report, conference papers, desertations etc. Vehicle model representative of two different passeneger cars were implemented using MATLAB-Simulink and a wheel power analysis was performed. The peak power data was collected for battery electric vehicles and other high selling passenger cars were collected and studied. Standard drive cycles were used along with the vehicle model. Using the result of wheel power analysis along with collected vehicle data and references, the design point for the high efficiency motor was finalized. The high efficiency motor was used as a reference for further design of the two more motors namely high power and centralized. The electric motor design were carried out using RMxprt, Ansys-Maxwell. The efficiency maps were generated using search algorithm in MATLAB. Intially, the electromagnetic designs were compared using, power, weight etc. The performance evaluation of the three motors were also done using different drive cycles using the vehicle model earlier design in Simulink.

2

Vehicle model and drive cycles

2.1 Vehicle Model

One dimensional vehicle model approximating the vehicle body as a rigid lumped mass around its centre of gravity will be used to dimension the powertrain components in a BEV. Using Newton's second law of motion, the linear motion of the vehicle can then be describe by

$$ma = m\frac{d}{dt}v(t) = F_{tractive}(t) - F_{resistive}(t) \tag{2.1}$$

where m is the mass of the vehicle in (kg), a in (m/s^2) is the acceleration of the vehicle, v(t) is the vehicle speed in (m/s), $F_{tractive}(t)$ and $F_{resistive}(t)$ are the forces supporting and opposing the vehicle motion respectively. The main tractive force exerted on the vehicle is produced by the propulsion system, an electric motor coupled with gearbox and may include the force due to gravity during downhill driving. The reactive forces opposing the motion of the vehicle is the result of aerodynamic drag produced by air around and through the vehicle body, the rolling resistance, regenerative and frictional braking along with the force due to gravity during uphill driving [6].

2.1.1 Aerodynamic drag

The aerodynamic drag is the resistance offered by the air surrounding the vehicle. The geometry of modern day automobiles require sophisticated wind tunnel measurement or complex CFD simulation to accurately measure or estimate the aerodynamic drag [6]. However, a rough estimation of the aerodynamic drag force, F_{aero}, can be made using the following equation

$$F_{aero} = \frac{1}{2}\rho_a C_d A_f (v_{car} - v_{wind})^2 \tag{2.2}$$

where ρ_a is the density of air in (kg/m^3), C_d is the aerodynamic drag coefficient, A_f is the effective frontal cross section area of the vehicle expressed in (m^2), v_{car} and v_{wind} expressed in (m/s^2) are the vehicle speed and the wind moving parallel to it respectively [15].

As seen from eq. 2.2, the aerodynamic drag increases with the wind speeds and can be significant at higher vehicle speeds. However, the wind speed direction is not always parallel and can be quite random during actual driving. The air density depends on atmospheric conditions such as temperature, humidity, pressure and geographic condition like altitude. Vehicle frontal cross section area can be estimated by using wind tunnel measurements or through the detailed drawings of the vehicle. Aerodynamic drag coefficient is a dimension less quantity that depends on the geometry of the vehicle, conditions such as open/closed window or roof in case of convertibles, direction of air flow etc. It can be determined using wind tunnel or coast down tests [15]. The recent trend has lead to decrease in aerodynamic drag coefficient to improve fuel efficiency of passenger cars [6]. The air moving around the vehicle also produces a side and lift force that causes a yawing and pitching moment [15]. It will be assumed that these forces have small impact compared to longitudinal drag mentioned above.

2.1.2 Rolling resistance

The tire geometry during a vehicle's motion is continuously deformed leading to an internal force opposing the motion. The internal force, F_{roll} is called the rolling resistance. It is the main resistive force at low speed and hard pavements. The rolling resistance force can be expressed as

$$F_{roll} = C_r mg \cos(\alpha) \tag{2.3}$$

where C_r is a dimensionless quantity called rolling resistance coefficient, m is the vehicle mass in (kg), g expressed in (m/s^2) represents the acceleration due to gravity and α is the road inclination angle [15].

As explained in [6], the $\cos(\alpha)$ is often neglected as the loss in accuracy even with a large road inclination is very less. The rolling resistance coefficient represents the interaction between the tire and ground and depends on several factors such as tire temperature, pressure, vehicle speed etc. However, in this study a constant value will be used as also mentioned in [6].

2.1.3 Gradient Force

The gradient force, F_{grad}, is the result of road inclination angle. It is equal to the component of gravitation force acting on vehicle parallel to the road surface and is expressed as

$$F_{grad} = C_r mg \sin(\alpha) \tag{2.4}$$

where the road inclination angle α in (rad/s) is the angle between the road surface and the horizon. The inclination angle is commonly expressed in terms of $\%grade$ as below

$$\alpha = \arctan(\frac{\%grade}{100}) \tag{2.5}$$

The gradient force, as explained earlier can either be resistive or tractive force depending on whether the vehicle is driven uphill or downhill respectively [6].

2.1.4 Wheel Force

The force required to sustain vehicle motion and to overcome all the resistive forces is called the wheel force and is equal to

$$F_{wheel} = F_{acc} + F_{aero} + F_{roll} + F_{grad} \tag{2.6}$$

where F_{acc} in (N) is the force required to accelerate the vehicle and from eq.2.1 is equal to

$$F_{acc} = ma = m\frac{d}{dt}v(t) \tag{2.7}$$

During vehicle acceleration, the wheel force is positive, while a negative wheel force indicates braking or deceleration. The limitation on maximum wheel force that can be exerted on the driving wheels is governed by the capacity of the powertrain or the friction available between the tire and the ground. If, F_{normal} is the the normal component of the force acting on the driving wheel and μ is the co-efficient of friction between the tire and road, then the maximum wheel force that will not result in tire spin or slip is given by

$$F_{wheel(max)} = \mu F_{normal} \tag{2.8}$$

The normal component of the force on the wheels depend on the weight distribution and may vary from vehicle to vehicle. The friction co-efficient is a function of longitudinal vehicle slip [6]. However, for the purpose of this thesis, the longitudinal tire slip will be ignored.

2.2 Drive Cycle

A drive cycle containing vehicle speed data over time represents a typical driving pattern for a particular road types. Drive cycles can be used to understand the static and dynamic loads experienced by the vehicle during use phase. The driving pattern in the real world can vary depending on driver behaviour, geographical location, weather or traffic conditions. Many studies have been conducted by regulatory authorities such as US Environmental Protection Agency, California Air Resource Board and United Nations Economic Commission for Europe to design standard test procedures representative of typical real-world driving to measure the fuel economy and regulated emissions in a laboratory environment. There are also, large projects such as WLTC, that is conducted to collect driving data using instrumented vehicles [6].

2.2.1 Legislative

The legislative drive cycles are used by regulatory authorities to measure fuel economy and regulated vehicular emissions for type approval testing. The legislative cycles varies from market to market. In the US FTP-75, SC03, UDDS, US06 and LA92 are used for fuel economy and CO_2 emissions measurement. Europe uses the

NEDC cycle for measuring fuel economy as well as other vehicular emissions. The NEDC cycle is the combination of ECE and EUDC cycles. Similar to Europe, Japan uses the JC08 cycle for regulatory tests [6].

2.2.2 Non legistative

Due to the usage of different drive cycles worldwide for regulatory tests, a harmonized drive cycle is proposed for type approval fuel economy and emission measurements. It represents the driving pattern on a global scale and is called the World harmonized light duty driving test cycle (WLTC) [6].

2.2.3 Drive cycles as per road type

The road type characterizes the drive cycle based on speed levels as **ubran**, **rural** and **highway**. The details about this can be found in [6]. The various drive cycles used in this thesis are presented in fig 2.1 - 2.3 according to road types.

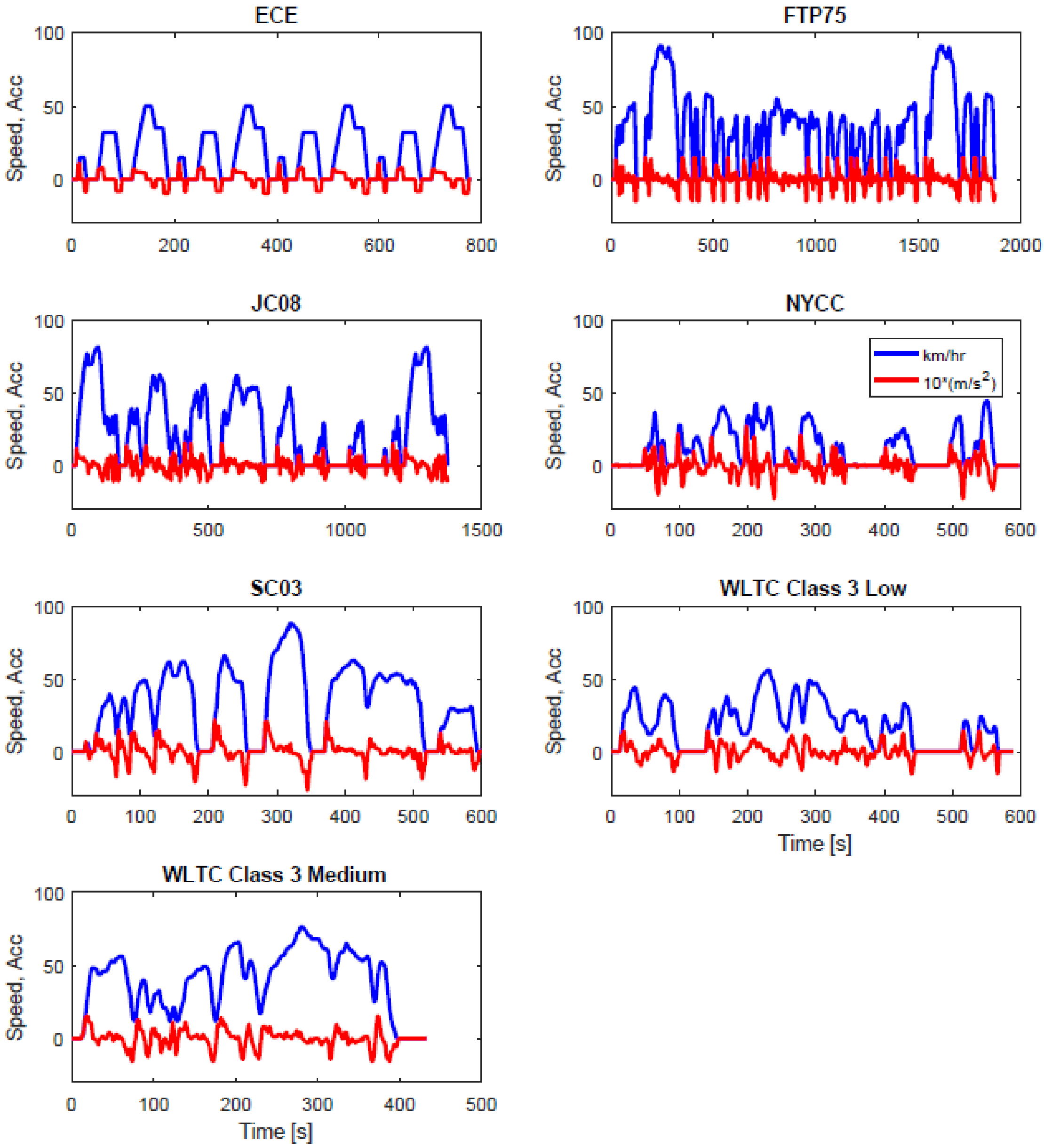

Figure 2.1: Vehicle speed and acceleration time series data for urban road type [16], [17]

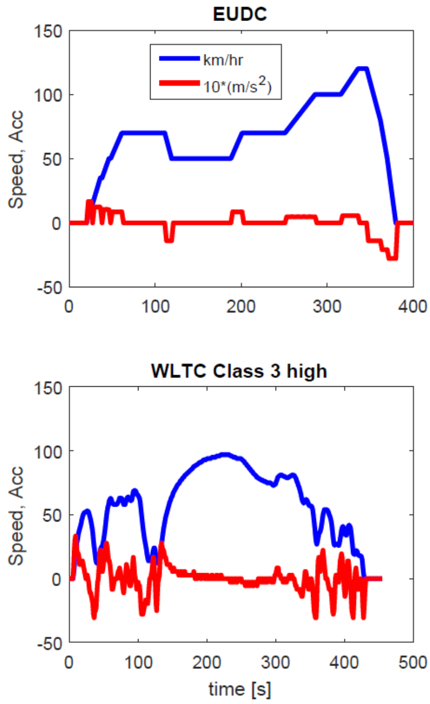

Figure 2.2: Vehicle speed and acceleration time series data for rural road type [16]

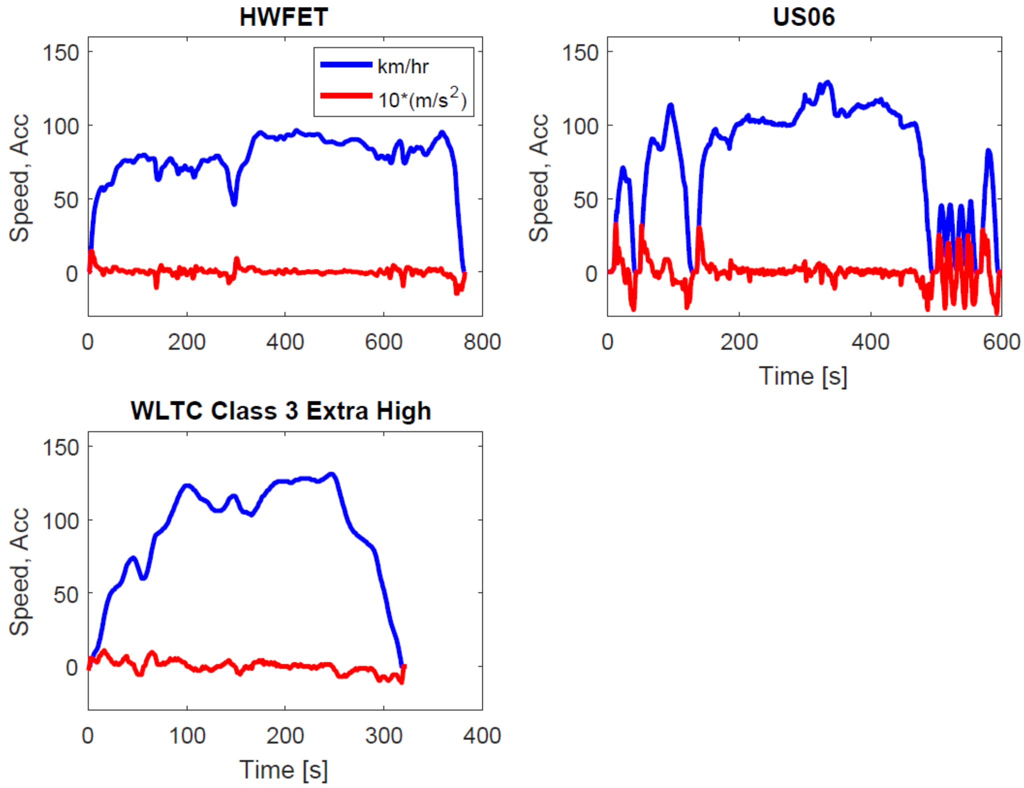

Figure 2.3: Vehicle speed and acceleration time series data for highway road type [16]

3

Electric Machine

3.1 Permanent magnet synchronous machine (PMSM)

A PM motor is the most common choice for electric propulsion system due to high efficiency and higher power and torque density. Some of the popular EVs using a PM motors are Fiat 500e, Chevrolet Spark EV, Volkswagen e-Golf, Ford Focus EV [6](Appendix A) and the newly launched Chevrolet Bolt [18]. A PM motor as the name suggest uses rare earth permanent magnets in the rotor to produce the rotor flux. The rotor and stator core uses laminated steel to reduce circulation of eddy currents. Depending on the arrangement of magnets on the rotor, various rotor designs are possible. Two of the main type of geometries are surface and insert mounted and are shown in fig 3.1. In the surface mounted rotor design, the magnets are glued to the surface which makes it mechanical inferior compared to insert mounted for high speed application like electric vehicles.

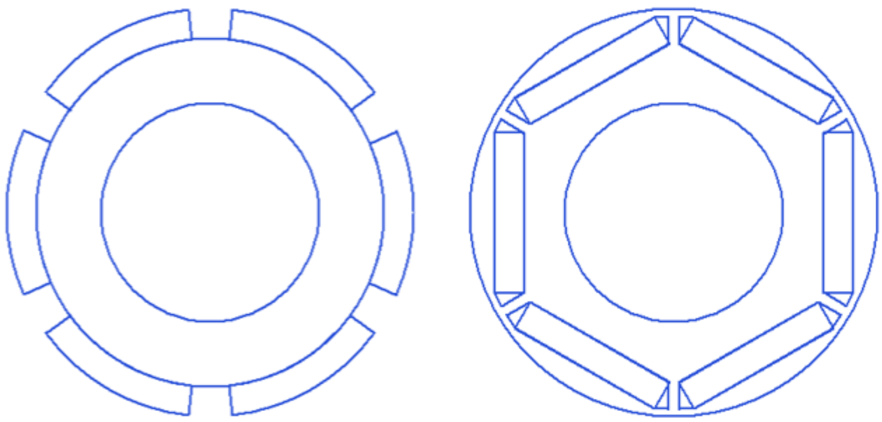

Figure 3.1: Permanent Magnet rotor types: surface mounted and insert mounted

3.1.1 PMSM Model

The dq model using synchronous coordinate system is a commonly used representation of a PMSM. The stator voltage equations in the steady state can be expressed as

$$u_d = R_s i_d - \omega_r \Psi_q \tag{3.1}$$

$$u_q = R_s i_q + \omega_r \Psi_d \tag{3.2}$$

where R_s is the stator winding resistance, i_d and i_q are the stator currents in d and q direction respectively and ω_r is the electrical rotor angular speed. Ψ_d and Ψ_q represents the total flux linkage in the d and q direction including the end winding effect as follows

$$\Psi_d = \Psi_{d_0} + L_{end} i_d \tag{3.3}$$

$$\Psi_q = \Psi_{q_0} + L_{end} i_q \tag{3.4}$$

where L_{end} represents the end winding inductance. Ψ_{d_0} and Ψ_{q_0} can written as

$$\Psi_{d_0} = \Psi_m + L_d i_d \tag{3.5}$$

$$\Psi_{q_0} = L_q i_q \tag{3.6}$$

where L_d and L_q are the d and q winding inductances and Ψ_m is the flux linkage due to the permanent magnets. Ψ_{d_0} and Ψ_{q_0} can be directly obtained from FEM simulations for various operating points using the 3ϕ flux linkages via abc to dq transformations. Now, the electromagnetic torque produced by the machine while using amplitude invariant transformation can be written as

$$T_e = \frac{3}{2} n_p (\Psi_d i_q - \Psi_q i_d) \tag{3.7}$$

where n_p is the number of pole pairs [6].

3.1.2 PMSM Losses

The main losses in a permanent magnet machine are resistive losses in the stator winding and core losses in the iron core. Apart from this, there are mechanical losses due to air and bearing friction, eddy current losses causes by circulating eddy currents in the iron and stray losses as a result of leakage flux.

The **copper losses** depends on the stator winding resistance, R_s and the RMS value of the stator current. Using dq currents, the Cu-loss can be expressed as

$$P_{cu} = \frac{3}{2} R_s ({i_d}^2 + {i_q}^2) \tag{3.8}$$

The stator winding resistance is a function of temperature. Hence, the Cu-losses in the machine increases with temperature for the same value of stator current. There are other effects such as proximity and skin effects that also affect the resistance of the winding [6]. However, in this thesis stranded conductors are used and is assumed that proximity and skin effect can be neglected .

The **core losses** in the iron are the result of magnetic hysteresis and induced eddy currents. The core losses can be expressed as function of peak flux density and frequency as

$$P_{core} = k_h f {B_{peak}}^n + k_c f^2 {B_{peak}}^2 \tag{3.9}$$

where k_h and k_c are hysteresis and eddy current parameter and can estimated using the B-H curve of the iron material in FEM software. B_{peak} is the peak flux density in the B-H curve, f is the frequency of the flux and n depends on B_{peak}, f and steel material [6]. Due to the complexity involved in calculation of core losses, a simpler approach is followed where the core losses are calculated for one operating point using FEM tools and scaled to estimate the core losses for other operating points as follows

$$P_{core} = \frac{\Psi^2(k_h f + k_c f^2)}{{\Psi_{FEM}}^2(k_h f_{FEM} + k_c {f_{FEM}}^2)} P_{core(FEM)} \tag{3.10}$$

It is clear that eq 3.10 is derived by substituting n=2 in eq 3.10 and the subscript FEM indicates the operating point where the core-losses are calculated using FEM software.

Similarly, the **stray** and **mechanical losses** can be assumed to be 0.5% of the peak power and scaled up for the other operating point as

$$P_{mech} = \frac{5}{1000} P_{peak} \frac{\omega^2}{{\omega_{base}}^2} \tag{3.11}$$

$$P_{stray} = \frac{5}{1000} P_{peak} \frac{{I_s}^2 \omega}{{I_{s(peak)}}^2 \omega_{base}} \tag{3.12}$$

where P_{peak} is the peak power of the machine and ω_{base} is the base speed of the machine. The base speed is defined as the speed at which the machine is operating at its maximum power limit i.e. maximum stator voltage and current.

3.1.3 Operating region boundary

The maximum torque per ampere (MTPA) is a rather simple strategy that can be used to find the optimal operating region boundary for a PMSM. As the name indicates, the current angle ($\tan^{-1}(\frac{i_q}{i_d})$) is selected so as to obtain the maximum torque for a given amplitude of the current. The operating boundary of the PMSM based on control strategy is shown in fig 3.2. The dashed line indicates the base speed of the machine. In the first section indicated by MTPA, the current is selected to be maximum limited by the inverter capacity and negative Ψ_d which can cause demagnetization of the magnet. In the second region, the MTPA strategy is followed till the voltage limit of the inverter is reached beyond which another strategy called the maximum torque per voltage (MTPV) is followed. In MTPV, the optimal current angle is obtained for which the voltage is within the inverter voltage limit.

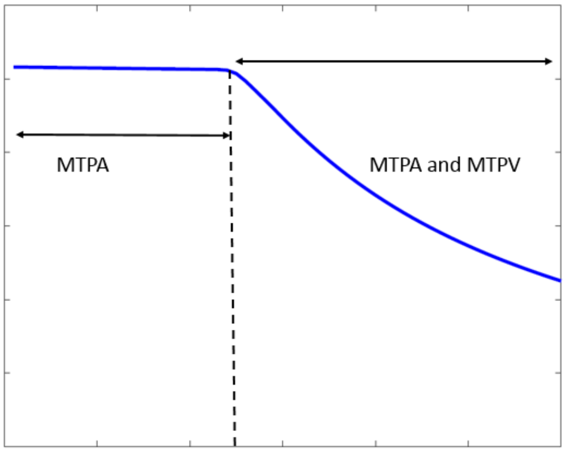

Figure 3.2: Torque speed operating boundary of a PMSM

3.2 Electromagnetically excited synchronous machine (EESM)

An EESM as shown in fig 3.3 ,uses DC current in rotor windings to produce the rotor flux. The stator windings are similar to that of PMSM. The rotor currents leads to additional losses but it also provides an additional degree of freedom for control and eliminate the need to use rare earth magnets. EESM have the additional advantage of having higher torque at low speed compared to interior mounted PMSM, wider constant power speed region, high overload capablity and better power factor at peak power [20]. It can be a better alternative to PMSM if peak power and high torque at lower speed is required.

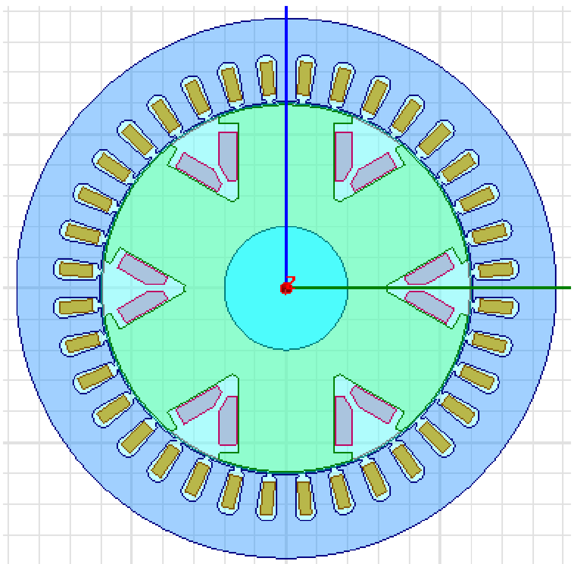

Figure 3.3: An EESM with claw pole rotor

3.2.1 EESM Model

The EESM model in dp is quite similar to that of PMSM and the same eq 3.1 - 3.3 and 3.6 can be used. The difference is in Ψ_{d_0} which for an EESM can be written as

$$\Psi_{d_0} = L_m i_{exc} + L_d i_d \tag{3.13}$$

where L_m is the mutual inductance and I_{exc} is the field excitation current. The excitation voltage and the excitation flux linkage in steady state can be expressed as

$$U_{exc} = R_{exc} i_{exc} \tag{3.14}$$

$$\Psi_{exc} = \frac{3}{2} L_m i_d + L_{exc} i_{exc} \tag{3.15}$$

where R_{exc} is the resistance of the field winding and L_{exc} is the self inductance. The electromagnetic torque can be calculated using the same as in eq. 3.7 [21].

3.2.2 EESM losses

Due to the use of field winding, the EESM has additional copper losses in the rotor. The copper losses can be obtained as

$$P_{cu} = \frac{3}{2} R_s ({i_d}^2 + {i_q}^2) + {i_{exc}}^2 R_{exc} \tag{3.16}$$

Apart from this, the core, stray and mechanical losses can be obtained using the same equation as explained in section 3.1.2

3.2.3 Operating region boundary

The control strategy mentioned in [20] can be used to obtain the operating region boundary for EESM. MTPA will be used to operate the machine at maximum torque at low speed similar to PMSM with peak stator current and peak excitation current. At higher speed, the excitation current is reduced to operate the machine MTPA without exceeding the voltage limit. The excitation current control at higher speed leads to unity power factor operation in this machine.

4

Case Setup

4.1 Vehicle model

A vehicle model as described in chapter 2 is created in MATLAB/Simulink which is also used to dimension the electric machines. The data required to model the vehicle are taken from [6] (Table 4.2). The small and medium sized car models are used in this thesis and are also presented in table 4.1.

Table 4.1: Parameters used for modeling the vehicles

Vehicle parameters	Small	Medium
Mass (kg)	1200	1700
C_d	0.3	0.28
Area (m^2)	2.05	2.3
C_r	0.009	0.009
Wheel radius (m)	0.31	0.32

In all simulation, wind speed and gradient are considered 0 unless otherwise mentioned. This is done entirely to simplify the analysis. The time series data of the drive cycles contain only vehicle speed. Hence, the vehicle acceleration is derived by differentiating the vehicle speed. The central difference method as described in [6] (Page 67) is used in this work as it provides the most neutral estimation of the acceleration. The acceleration due to gravity, g is equal to 9.8 m/s^2 and the density of air is assumed to be 1.225 kg/m^3.

4.2 Time step and meshing

The time step used in FEM tools impacts the accuracy of certain results. A smaller time step is preferred while calculating torque ripple or to include the impact of slot harmonics etc. On the other hand a larger time steps may be preferred to reduce the overall calculation time in FEM for one simulation. In this work, the design mainly focuses on the power and losses, a very high accuracy is not desired. So, the time steps are selected to include 100 calculation points in one electrical cycle e.g. if the electrical frequency is 200Hz

$$T_{step} = \frac{1}{100 * 200} = 50\mu s \tag{4.1}$$

It is a common practice to extract the core-losses from the second electrical cycle. Hence, two electrical cycles are simulated. Using a frequency of 200Hz as above it results in

$$T_{stop} = \frac{2}{200} = 10ms \tag{4.2}$$

Similarly, mesh element size also influences the accuracy of the field calculation. The maximum mesh element size for the 3 motors designed in this work are mentioned in table 4.2. As can be seen in table 4.2, the same mesh element size is used for the two different PMSMs. The EESM used in this work is designed using RMxpert and then the 2-D model is generated automatically for FEM simulation and hence, the mesh settings are retained. The mesh is refined for PMSM as shown in 4.1 between the rotor outer surface and magnet duct which is also called the bridge. This area is highly saturated and hence, a refined mesh will improve the results.

Table 4.2: Mesh element size

Parts	High Efficiency (PMSM)	High Power (EESM)	Centralized (PMSM)
Stator	4mm	5.6mm	4mm
Rotor	4mm	5.6mm	4mm
Coil	2mm	3.25	2mm
Magnet	3mm	NA	3mm

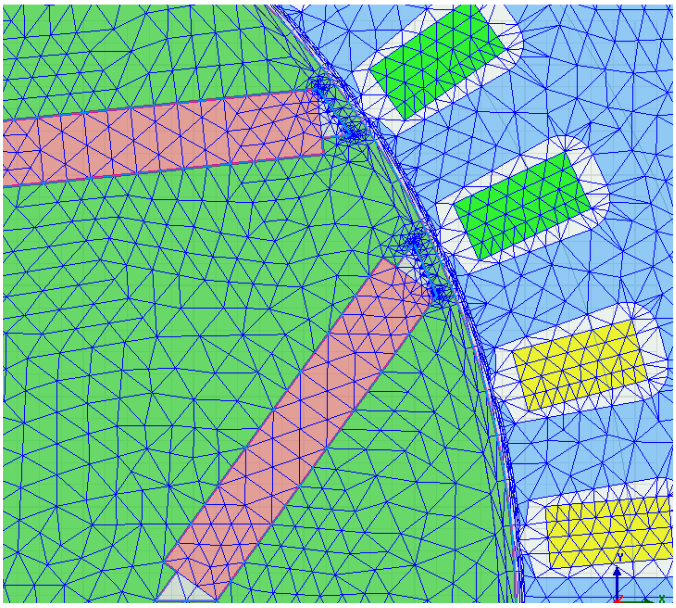

Figure 4.1: Mesh refinement near the magnet bridge

4.3 High efficiency motor simulation setup

As mentioned earlier, a PMSM is used as the high efficiency motor. The basic parameters used for the design of the motor are presented in table 4.3. A V-shape magnet geometry as shown in fig 4.2 is adopted in this work with reference to [6], [18] and [22]. The slot fill factor indicated in table 4.3 are obtained directly from Ansys RMxprt which takes into account the insulation on the copper wire. Hence, the actual copper fill factor is around 40%. However, the fill factor mentioned in table 4.3 will be used for calculating current densities.

Table 4.3: High Efficiency motor (PMSM) parameters used in design

Stator outer diameter	175mm
Airgap	0.8mm
Stack length	100mm
Shaft diameter	40mm
Number of poles	6
Number of slots	36
Fill Factor	50%
DC link	400V

The peak current is selected such that the machine can be operated at MTPA without having negative Ψ_d and accordingly the peak current density is calculated. The coil sequence used in the stator is B-A+C-. The phase A of the stator winding is aligned to the d-axis as shown in fig 4.2 at $t = 0$ and the initial angle for FEM simulation is 0. Current excitation in dq co-ordinate is used. If I_{amp} is the current amplitude and γ is the current angle, the d and q currents become

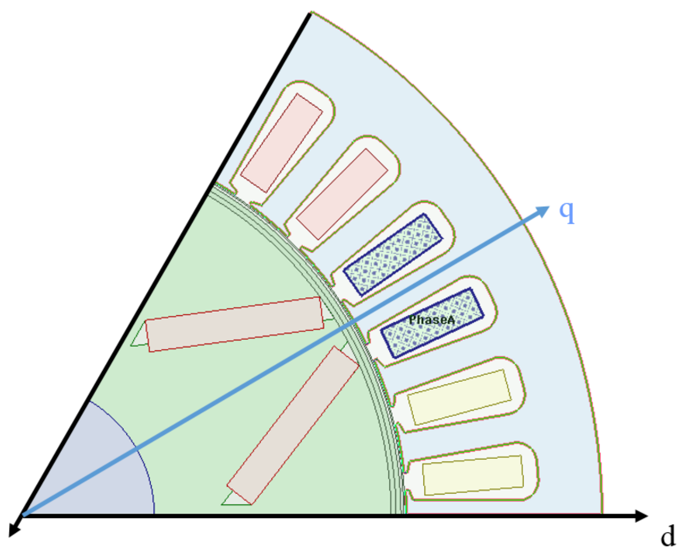

Figure 4.2: The dq axis in a PMSM with V-shaped magnets at $t = 0$

$$i_d = I_{amp}cos(\gamma) \tag{4.3}$$

$$i_q = I_{amp}sin(\gamma) \tag{4.4}$$

Using, the d and q currents, the phase current excitation can be obtained as

$$i_a = i_d cos(2\pi ft) - i_q sin(2\pi ft) \tag{4.5}$$

$$i_b = i_d cos(2\pi ft - \frac{2\pi}{3}) - i_q sin(2\pi ft - \frac{2\pi}{3}) \tag{4.6}$$

$$i_c = i_d cos(2\pi ft + \frac{2\pi}{3}) - i_q sin(2\pi ft + \frac{2\pi}{3}) \tag{4.7}$$

where f is the electrical frequency and t is the time.

4.4 High Power motor simulation setup

An EESM with a claw pole rotor as shown in fig 4.3 is used as high power motor. The parameters selected for design are presented in table 4.4. As seen in table 4.4, all parameters except airgap are kept same as that of PMSM to be able to compare the motors easily. The reason to use a slightly higher gap is to account for the fact that the additional field winding in case of the EESM will cause losses and hence more thermal expansion of the rotor.

Table 4.4: High Power (EESM) parameters used in design

Stator outer diameter	175mm
Airgap	1mm
Stack length	100mm
Shaft diameter	40mm
Number of poles	6
Number of slots	36
Fill Factor	50%
DC link	400V

The coil sequence in the EESM is A+C-B+ and as shown in fig 4.3, the axis of phase A is aligned towards the d-axis for a initial angle of 10°. The direction of the d-axis is determined by the excitation current. The maximum current density for both field and stator windings are kept at $30A/mm^2$. The current excitation for the EESM can be obtained using the same eq 4.3 - 4.7.

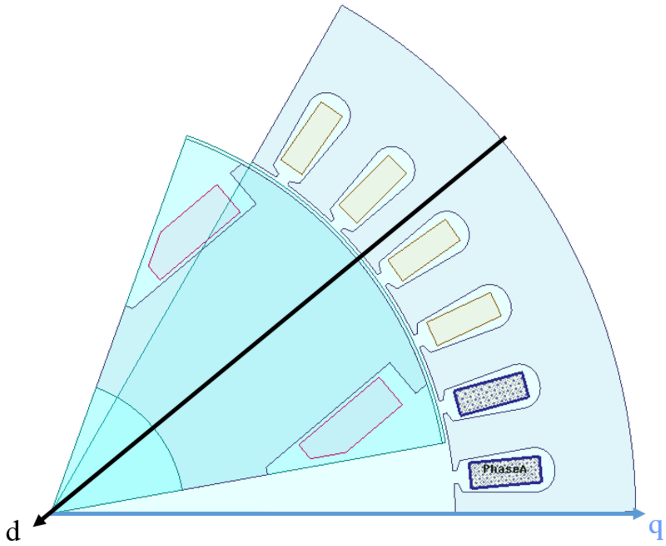

Figure 4.3: The dq axis in the EESM at $t = 0$

4.5 Centralized motor simulation setup

As already mentioned, a third motor is designed using PMSM as reference to compare the proposed design. The dimension of this machine is selected to have double the volume of the high efficiency motor while maintaining the same ratio between stack length and stator outer diameter as the high efficiency. The parameters selected for the design are shown in table 4.5. The airgap and shaft diameter as mentioned in table 4.5 are scaled up using the stator outer diameter. The same V-shape magnet geometry along with same number of poles and number of slots is used. The fill factor is also same as the other two machines.

Table 4.5: Centralized (PMSM) parameters used in design

Stator outer diameter	220mm
Airgap	1mm
Stack length	125mm
Shaft diameter	50mm
Number of poles	6
Number of slots	36
Fill Factor	50%
DC link	400V

The peak apparent power of this motor is selected to be the sum of the high efficiency and high power motors. Hence, the peak current is selected according to the available peak apparent power. The dq axis, the current excitation and the initial angle are same as the high efficiency motor.

5

Analysis

The main objective of the work is to compare the proposed design with the current conventional electric powertrain design. A analysis of peak power rating of the existing BEVs and internal combustion engine based vehicles was conducted followed by a wheel load analysis using two different vehicle models and standard drive cycles presented earlier. The machines geometry was then optimized according to the design point using iterative process. Finally, the various machines were then compared for performance.

5.1 Vehicle data

The specification of existing vehicles can be used as reference while dimensioning the power train of a vehicle. In [6], a wide range of electric vehicle datas are presented which is partly used in this work. However, apart from this the specification of ICE based vehicles is also used. Since, ICEVs have been around for a longer time than the EVs, it can be assumed that they are more performance optimized. In [6], the vehicles are classified as small, medium-large and sport which is retained for categorizing the BEVs. The ICEVs selected to represent the highest selling passenger vehicle are taken from [23] where they are classified as A segment, B segment, C segment and so on as per the European Commission's vehicle classification [24]. The ICEVs usually have a range of variants depending on the engine, transmission, peak power etc. Hence, for this study the models with the lowest engine peak power, base and the highest peak power, high is considered. The details of the selected vehicle data can be found in Appendix A

5.1.1 EVs and ICEVs performance comparison

The EVs and ICEVs selected in this study use different classifications which may make the comparison rather difficult. It was decided to compare the small EVs with the B segment ICEVs and the medium-large EVs with C segment ICEVs. The analysis is mainly based on peak power and curb weight.

5.1.1.1 Small EVs and B segment ICEVs

Fig 5.1 presents the peak power of the small EVs (e.g. Fiat 500e, Cheverolet Spark EV etc.) and the B segment ICEVs (e.g. Ford Fiesta, Volkswagen Polo etc.) along with the curb weight. The small EVs have peak power in the range of 47 - 60 kW except for Fiat 500e (83 kW) and Mitsubishi MiniCab (30 kW). Similarly, the base models of the ICEVs have the peak power in the range of 44 - 62 kW with the exception of Hyundai Accemt (102 kW). So, the small EVs compare well with the base models of the ICEVs in terms of peak power. It is worth noting that the curb weight of the EVs is on the higher side which may be due to the heavier battery pack. The ICEVs as mentioned earlier also have various performance options between the base and high end models. The high end models of these vehicles can have peak power as high as 162 kW (Renault Clio). The peak power of the high end models vary much more than the base models depending on the manufacturer and vehicles intended usage. The choice of having multiple power options can be considered an advantage which is currently not common in EVs.

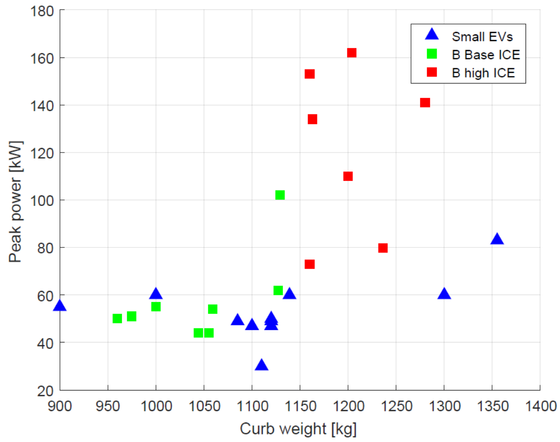

Figure 5.1: Peak power of small EVs and B segment ICEVs

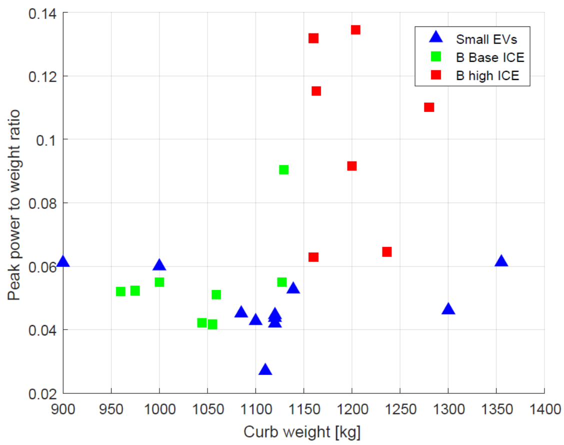

Figure 5.2: Peak power to curb weight ratio of small EVs and B segment ICEVs

The peak power to vehicle weight ratio can be attributed to the acceleration performance of the vehicle where a lower ratio indicates slower acceleration and vice versa. In fig 5.2, the peak power to weight ratio (kW/kg) is compared for both EVs and ICEVs. The base models and small EVs compare well and have the ratio in the range of 0.04-0.06. Due to the higher peak power in the high end models, the ratio is much higher leading to possibility of superior acceleration performance.

The comparison of the peak power and the ratio of the peak power to curb weight indicates that the small EVs are more adapted towards the base models in terms of performance.

5.1.1.2 Medium-Large EVs and C segment ICEVs

The peak power of medium-large EVs and C segment ICEVs is shown in 5.3. Unlike the small EVs, the medium-large EVs vary in terms of peak power and the range of peak power is much wider. It may be because this classification of EVs covers a more broader range of vehicles having much higher curb weight e.g. BYD e6 (2380 kg), Toyota RAV4 EV (1828 kg) etc. Most of the EVs in this category have a peak power in the range of 65 - 92 kW which is quite similar to the C segment ICEVs. The high end models like the B segment have varying peak power e.g. Volkwagen Golf (221 kW). The curb weight difference is more visible in this segment of EVs which might be due to larger battery packs needed in these EVs to support long range driving. The peak power of the EVs and ICEVs indicates that the EVs in this category are comparable to both base and high end models of the ICEVs.

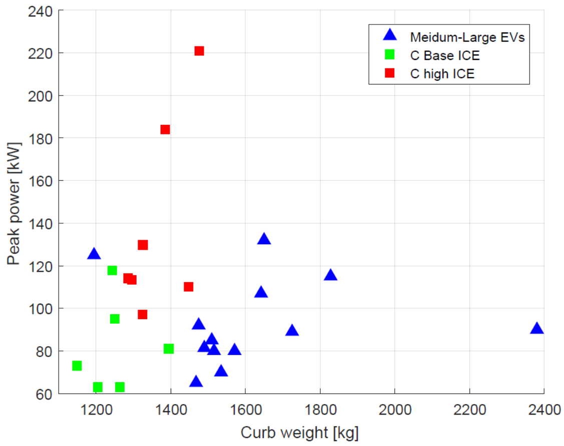

Figure 5.3: Peak power of medium-large EVs and C segment ICEVs

Even though the peak power of the EVs in this category are comparable to the ICEVs, the peak power to weight ratio is slightly on the lower side as shown in 5.4 which is due to higher curb weights generally seen in the EVs in this category.

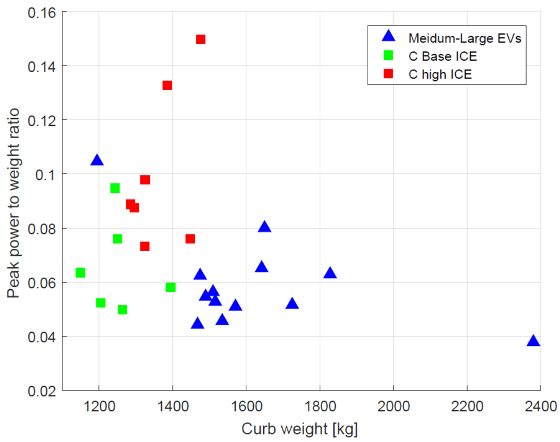

Figure 5.4: Peak power to curb weight ratio of medium-large EVs and C segment ICEVs

5.2 Wheel load analysis

The analysis of the vehicle data gives a fairly good idea of defining the peak power requirements based on vehicle category. However, it fails to explain the various aspect of the driving usage that define these requirements. This can be evaluated by understanding the load on the driving wheels of a vehicle which can be represented by wheel power. Vehicle models were created for a small and medium car for which the data is provided in section 4.1 using the method describe in section 2.1. The propulsion, braking, average power etc was studied for the drive cycles shown in fig 2.1, 2.2 and 2.3.

5.2.1 Small car wheel power analysis

The peak power required for a small car to fulfill the various drive cycle is presented in table 5.1. The results presented in table 5.1 for propulsion and braking peak power is represented by positive and negative peak power respectively. Beside this, a normal distribution of power sample values was also analysed e.g. the wheel power sample value distribution of the small car in ECE drive cycle is shown in fig 5.5. Using the normal distribution, the power required to meet 90% and 80% of the drive cycle is calculated as the percentile value and is also presented in table 5.1. The average power calculated for various drive cycle does not include the idling time.

The peak power required for completing the drive cycle for the small car is below 40kW except the braking power in UC LA92 cycle and the propulsion power in US06 cycle. In contrast to the peak power, the average power is very low with a maximum of around 12 kW for WLTC Extra High cycle. The driving power required for 90% of the time is even below 13 kW (city), 16 kW (rural) and 28 kW (highway) which indicates that the main requirement for peak power usually comes from the acceleration requirements of these drive cycles e.g. US06 drive cycle has the highest acceleration requirement ($3.2m/s^2$) and the UC LA92 drive cycle has the highest deceleration requirement ($-3.9m/s^2$). The average power corresponds to the average speed e.g. WLTC Extra High drive cycle with the highest average power also has the highest average speed (excluding idle time) of 94 km/hr.

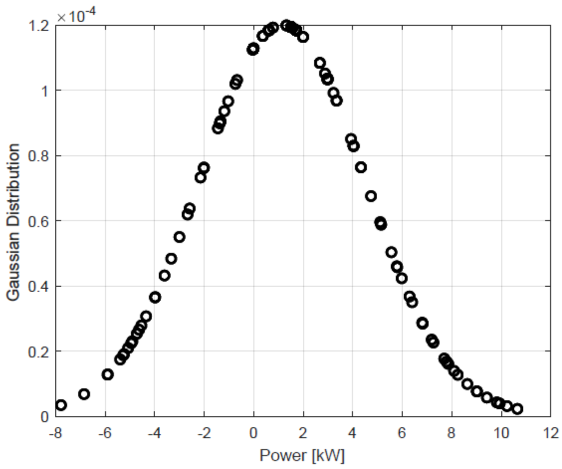

Figure 5.5: Normal distribution of power sample values for ECE drive cycle using a small car

Table 5.1: The wheel power analysis data for a small car

Drive cycle		Peak Power (kW)		Percentile P (kW)		Average Power (kW)
		Positive	Negative	90th	80th	
city	ECE	10.15	8.06	5.71	2.48	1.43
	NYCC	26.98	14.80	5.39	2.32	1.43
	FTP75	28.05	17.67	9.44	6.22	2.58
	WLTC Low	17.45	10.01	6.93	3.67	1.38
	SC03	31.09	25.05	12.25	6.99	2.97
	WLTC Medium	24.97	20.29	12.29	7.67	2.78
	JC08	16.79	14.32	9.05	5.84	2.26
Rural	EUDC	28.59	19.97	15.99	11.21	5.99
	UC LA92	37.87	49.14	15.38	11.08	4.12
	WLTC High	25.08	20.67	13.40	11.08	4.85
Highway	HWFET	21.98	25.16	12.63	10.33	6.63
	US06	63.98	30.84	27.14	21.08	10.36
	WLTC Extra High	36.95	16.94	27.59	23.43	11.82

The ECE and EUDC drive cycle also have a small duration of cruising (constant speed driving) which can be used to calculate rated/continuous power of the powertrain. The power required to drive the small car at 50 km/hr and 120 km/hr are 2.5 kW and 17.5 kW respectively. The increase in power requirement of high speed driving is mainly due to increase in the aerodynamic drag. The maximum rated power is thus less than half of the peak power required in the drive cycles. The peak power required as per the wheel power analysis is slightly lower compared to the specification of similar small EVs or B segment ICEVs. This can be either due to the use of simplified vehicle models and standard drive cycles or that the additional peak power available is to fulfill other driving requirements e.g. the acceleration performance defined by manufacturer, driving on a gradient etc.

5.2.2 Medium car wheel power analysis

Table 5.2 presents a similar analysis performed on a medium car. The peak power requirement of the medium car is as expected higher due to the higher curb weight. Significant increase in the peak power is seen for the cycles with higher acceleration requirements. The maximum increase in propulsion power is observed in the US06 drive cycle and braking power in UC LA92 drive cycle where the impact of vehicle weight is more prominent. However, there is not much increase in the 80^{th} percentile power compared to the small car with a maximum increase of around 5 kW. Similar observations can be made also in increase of average power requirements of the medium car compared to small car where the increase is less than 2 kW. Also, the power required to drive at constant speed of 50 km/hr and 120 km/hr are 3.14 kW and 19.6 kW respectively.

Table 5.2: The wheel power analysis data for a medium car

Drive cycle		Peak Power (kW)		Percentile P (kW)		Average Power (kW)
		Positive	Negative	90th	80th	
City	ECE	14.00	11.48	8.02	3.14	1.91
	NYCC	38.05	21.06	7.58	3.24	1.97
	FTP75	39.15	25.24	14.65	9.14	3.73
	WLTC Low	24.41	14.26	9.72	5.16	1.86
	SC03	43.67	36.13	16.64	9.24	3.82
	WLTC Medium	35.11	29.10	16.79	10.50	3.59
	JC08	23.70	21.13	12.36	7.97	2.89
Rural	EUDC	35.35	29.42	19.61	15.27	7.10
	UC LA92	52.81	71.24	20.39	14.86	5.14
	WLTC High	35.17	29.65	17.72	14.31	5.88
Highway	HWFET	30.49	36.21	16.15	12.91	7.84
	US06	89.10	44.35	37.27	26.52	12.16
	WLTC Extra High	47.82	24.81	34.34	28.90	13.47

It can be inferred that even though the medium car has higher peak power requirement, the driving power required for most part including constant speed driving is not so different for the small and medium cars. If we assume that the vehicle parameters and drive cycles used in the study represent the real world use case, then it will be fair to say that the beside acceleration requirement, most of the driving load on the wheel does not change much between vehicle categories. The results of the medium car analysis when compared with specifications of vehicles presented in section 5.1.1.2 has more variations. It can be assumed that since the vehicles in this category are highway capable, they may need to have better acceleration performance compared to a small car. As it is observed that acceleration performance mainly affects the peak power. The difference in the peak power obtained in wheel power analysis and the vehicle specifications can be justified by the higher acceleration requirements defined for this category of vehicles by the manufacturer.

5.2.3 Impact of wind speed and road gradient on medium car

In the above two analysis, the wind speed and road gradient was assumed to be zero. The reason being that wind speed direction is fairly random and road gradient data are not available for the drive cycles used. In order to understand the impact of wind speed and road gradient a rather crude approach is taken.

The impact of wind speed on the positive peak power is studied assuming a head wind speed of 5m/s, 10m/s and 20m/s during the complete drive cycle duration and is presented in table 5.3. The wind speed impact is studied only for rural and highway drive cycles with the assumption that the chances of having high wind speed is more in such road types. The % increase is calculated to see the impact of head wind speed of 20m/s compared to no wind. The increase in the peak power for all drive cycle is similar in the range of 3-5 kW with the maximum increase in WLTC extra high (10.5%) and EUDC cycles (14.9%). The constant driving power calculated for 120 km/hr from the EUDC cycle is 24.8 kW, an increase of almost 5 kW. It is similar to the increase in peak power but considering that the continuous power is usually half of the peak power, it might be significant. So, the impact of long duration of head wind should be considered while the continuous rating of the powertrain.

Table 5.3: The peak positive wheel power in presence of head wind for medium car

Drive cycle		Peak positive power (kW)				% Increase
		0 m/s	5 m/s	10 m/s	20 m/s	
Rural	EUDC	35.35	35.68	36.66	40.61	14.88
	UC LA92	52.81	52.99	53.52	55.68	5.43
	WLTC High	35.17	35.31	35.71	37.32	6.11
Highway	HWFET	30.49	30.65	31.15	33.13	7.97
	US06	89.10	89.32	89.97	92.62	3.95
	WLTC Extra High	47.82	48.13	49.08	52.86	10.54

Similar to wind speed, a road gradient of 6% is applied simulating an uphill driving during the complete duration of the city drive cycles. The rural and highway drive cycles are not considered as higher road gradients are unusual for higher speed driving [6] (Page 47). The impact on the positive peak power is only considered and the results can be seen in table 5.4. It is evident that road gradient can have huge impact on the peak power requirement. The increase in the drive cycle power is around 10 - 16 kW with the maximum absolute increase in JC08 cycle (16.5 kW) and % increase in ECE drive cycle (99%). Apart from this the constant speed driving at 50 km/hr demands a power of 17 kW which is more than 5 times of that required in a level road (3.14 kW). This indicates that road gradients not only affect the peak power dimension of the powertrain but also the fractional overload capacity e.g. 30 sec or 60 sec power of the electric machine.

Table 5.4: The peak positive wheel power of medium car during uphill driving

Drive Cycle	Peak power (kW)		% Increase
	Level road	6% grad	
ECE	14	27.88	99.14
NYCC	38.05	48.68	27.93
FTP75	39.15	55.31	41.28
WLTC Low	24.41	37.45	53.42
SC03	43.67	57.52	34.00
WLTC Medium	35.11	47.59	35.54
JC08	23.70	40.20	69.62

5.3 Design of high efficiency machine

Using the analysis of BEV and ICEV specifications and the wheel power, the design point for the high efficiency machine are defined and presented in table 5.5. The high efficiency region is selected to cover the continuous driving power required for a highway drive for both small and medium car and also full-fill the most of the city and rural driving requirements. The peak power is also sufficient to fulfill most of the drive cycle requirement of both small and medium car.

Table 5.5: Design criteria for high efficiency machine

Design criteria	Specification
Speed (rpm)	4000
High efficiency region	10 - 20 kW
Efficiency	96%
Rated power	>25 kW
Peak power	>45 kW
Maximum Speed (rpm)	12000

The design criteria mentioned in table 5.5 along with the preliminary machine data presented in table 4.3 was used to finalize the design of the high efficiency machine. The final machine geometry can be seen in Appendix B. A no-load design was initially carried out to obtain initial geometry and then it was optimized at the maximum efficiency point.

5.3.1 No load performance

The magnetic flux density distribution of the final design at no load is shown in fig 5.6. The flux density in the magnet rib edges appear to be saturated due to high flux density. This will force the magnet flux to go via the teeth rather than leaking over it. This can be confirmed by observing the flux density vectors in fig 5.7 where most of the flux from the magnet passes through the stator teeth.

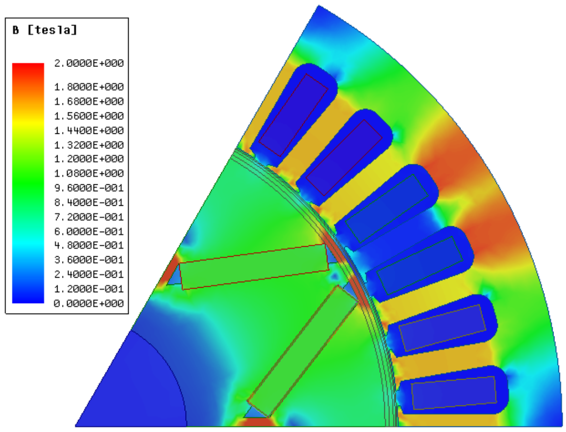

Figure 5.6: Magnetic flux density at no-load and t=0

The flux density in air gap, stator teeth and stator yoke is also calculated for no load operation. The maximum air gap flux density is 0.944 T which can be considered to be a bit higher. The maximum stator teeth and yoke flux density are 1.63 T and 1.86 T. The high flux density in the stator yoke is supported by the concentration of flux line in the stator yoke as seen in fig 5.7. The higher flux density during the no-load operation is the result of increase magnet use in order to achieve high efficiency.

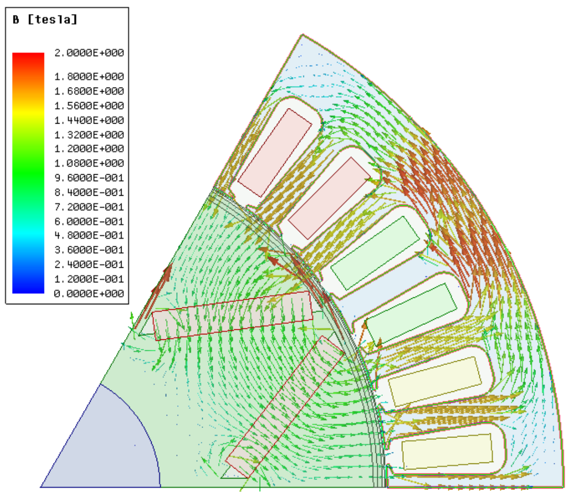

Figure 5.7: Magnetic flux density vectors at no-load and t=0

Fig 5.8 show the flux linkage and the induced voltage at no-load respectively. The flux linkage in phase A is maximum at $t = 0$ which confirms that the d-axis is in fact aligned to phase A as shown in fig 4.2. The flux linkage amplitude is 0.149 Wb. The induced voltage at 4000 rpm has a amplitude of 188V as shown in 5.8.

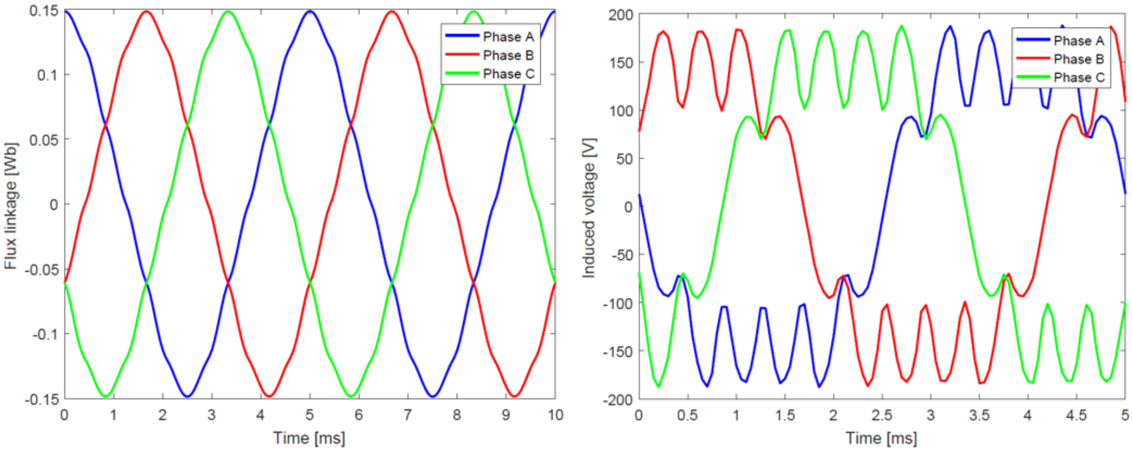

Figure 5.8: Three phase flux linkages and induced voltage at no-load and 4000 rpm

5.3.2 Flux Linkage Map

A map was created for d and q flux linkages by calculating the flux linkages for a finite number of i_d and i_q in FEM as shown in fig 5.9. Then using interpolation, the flux linkages can be calculated for any values of i_d and i_q inside the operating boundary. The stator voltage and electromagnetic torque can subsequently be calculated as described in section 3.1.1. The d flux linkage in fig 5.9 is higher for lower value of i_d which confirms with eq 3.5. A negative d current will cause weakening of the magnet flux and reduced d-flux linkage. Similarly, the q flux linkage in fig 5.9 usually increases with higher i_q in agreement with eq 3.6.

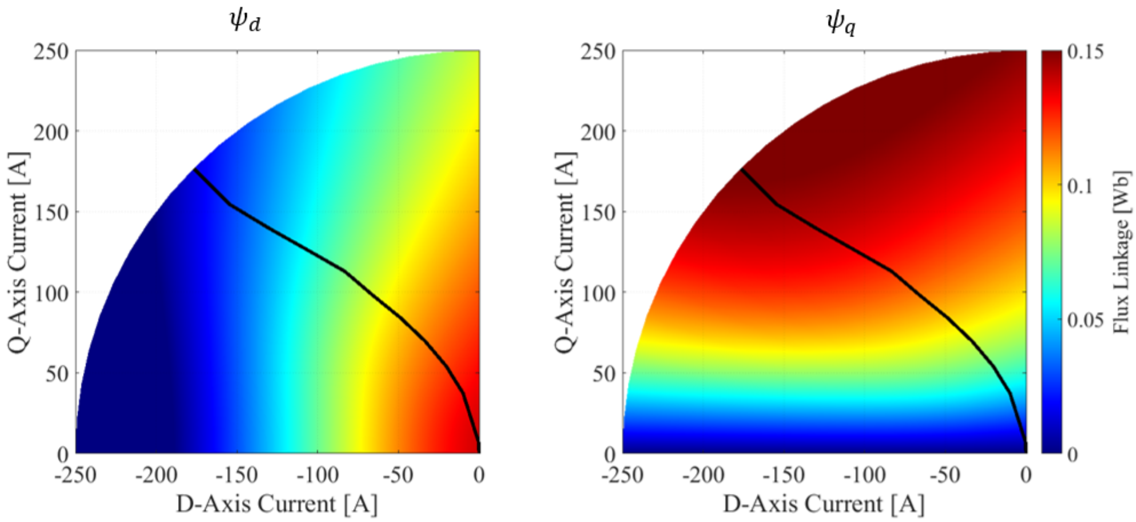

Figure 5.9: D and Q flux linkage maps with MTPA line

However, the impact of cross saturation is also visible in the flux linkage maps e.g. the d flux linkage reduces gradually as i_q increase especially for smaller values of i_d and similar observation can be made with the q flux linkage map. The flux linkage maps are used to find the operating points of the machine using MTPA and MTPV. The MTPA line in black is also shown in fig 5.9.

5.3.3 Efficiency map

The flux linkage map along with a searching algorithm is then used to calculate optimal stator current and current angle γ using MTPA and MTPV for around 2400 operating points inside the operating boundary of machine. The losses were in turn used to calculated the efficiency of the operating points and the result is presented in fig 5.10. The peak torque is 132 Nm and extend beyond the design speed of 4000 rpm which is due to the under utilization of stator voltage in a base speed of 4600 rpm. This indicates that by utlizing higher number of turns the peak torque can further be increased. However, the main design aim is to achieve higher efficiency and hence, it was not considered. The maximum efficiency is around 96% meeting the designed target. However, the high efficiency region with efficiency greater than 95% extends from 15 - 35 kW or (36 - 84 Nm) at the designed speed. The peak and rated power of the machine at the base speed are 63 kW and 40 kW respectively. The increase rated and peak power is the result of very high magnet amount used to achieve higher efficiency.

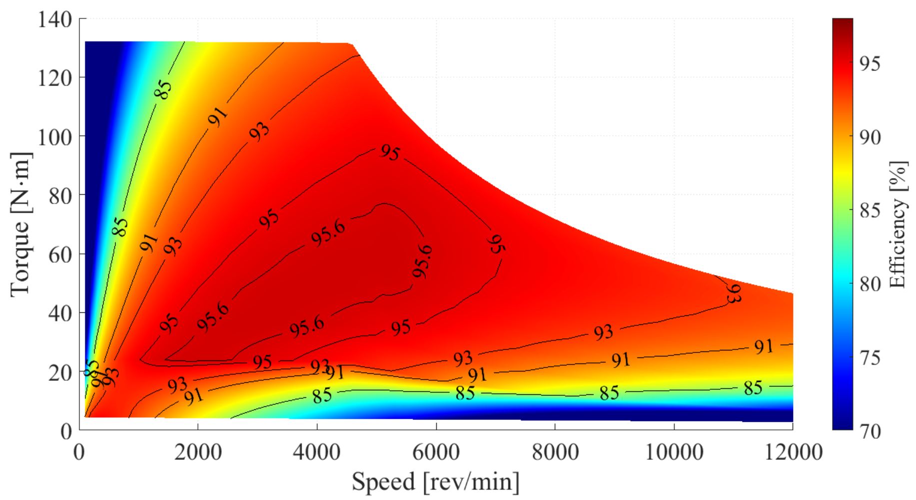

Figure 5.10: Efficiency map of the high efficiency machine

5.4 Design of high power machine

The high power machine was designed with the aim to provide very high overloading capability with a good power factor at peak power. The outer dimension of this machine was selected to be the same as shown in table 4.4. Unlike PMSM, there are no magnets and hence the limitation on current is mainly defined by thermal capabilities. Since, the machine is designed to deliver peak power capabilities, the ratio of stator Cu to iron area, 0.15 is almost half compared to high efficiency machine which is 0.302 and can also be observed in fig 5.11.

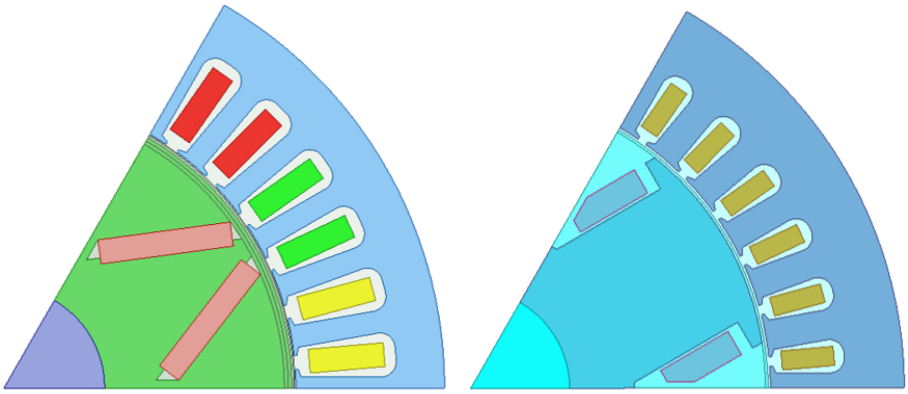

Figure 5.11: Cross section of the high efficiency and high power machine

5.4.1 No load performance

The no load flux density distribution and flux lines were studied similar to the high efficiency machine and can be seen in fig 5.12 and 5.13. The no-load flux density distribution indicates that both the teeth and yoke are saturated. The peak flux density values are 1.36 T, 1.93 T and 2.05 T for airgap, stator teeth and stator yoke flux densities. Compared to the high efficiency machine these values are considerably higher. The flux density vectors in fig 5.13 show a different pattern from fig 5.7 as the flux path appear to be closed via the inner rotor as well as the shaft. However, the edges and the middle portion of the pole shoe contribute less to the magnetic circuit where the flux density is much lower compared to the pole body. But, a wider pole shoe might be desired to provide mechanical support to the stoppers that are used to hold the field windings.

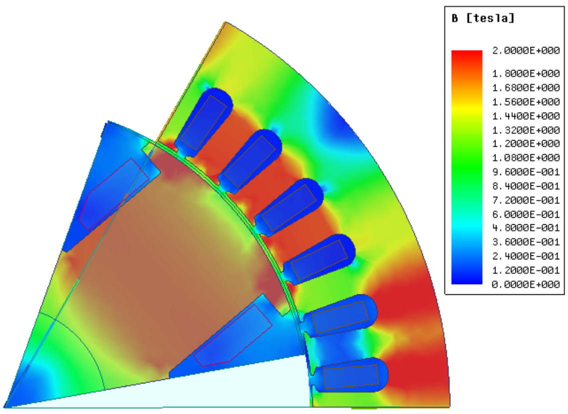

Figure 5.12: Magnetic flux density at no-load and t=0

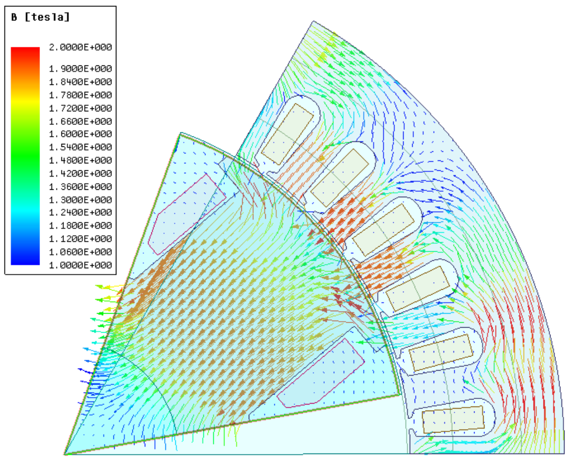

Figure 5.13: Magnetic flux lines at no-load and t=0

The three phase flux linkages and the induced voltages for the EESM are presented in fig 5.14. The flux linkage amplitude at 0.18 Wb is higher than the high efficiency machine and the flux linkage of phase A at $t = 0$ is maximum confirming the alignment of d-axis fig 4.3. The induced voltage at 4000 rpm has an amplitude of 205V as seen in fig 5.14.

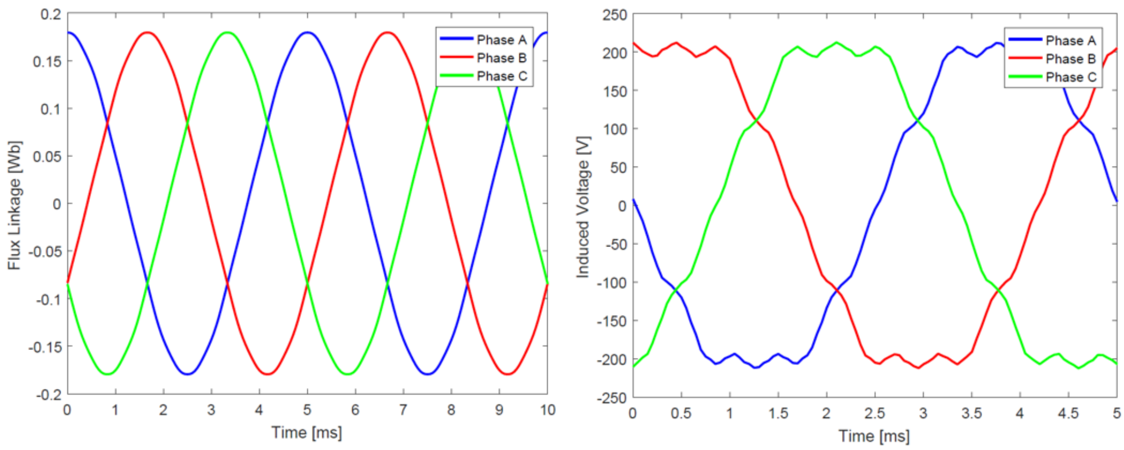

Figure 5.14: Three phase flux linkages and induced voltage at no-load and 4000 rpm

5.4.2 Flux Linkage Map

The flux linkage map in case of EESM is created for different field excitation current by calculating the flux linkages in FEM for a range of i_d, i_q and i_{exc}. Due to the additional degree of freedom i.e. i_{exc} the number of calculation points are multifold compared to PMSM. The d and q flux linkage map of the high power machine corresponding to zero and maximum excitation can be seen in fig 5.15 and 5.16. In case of PMSM, i_d is always negative. However, for EESM i_d can be positive for lower magnitude of stator current and hence the flux linkage maps in fig 5.15 and 5.16

ranges from $\gamma = 60°$ to $170°$. It can be observed in fig 5.15 that the d-flux linkage is almost zero for no excitation except when i_d is positive. So, the contribution to

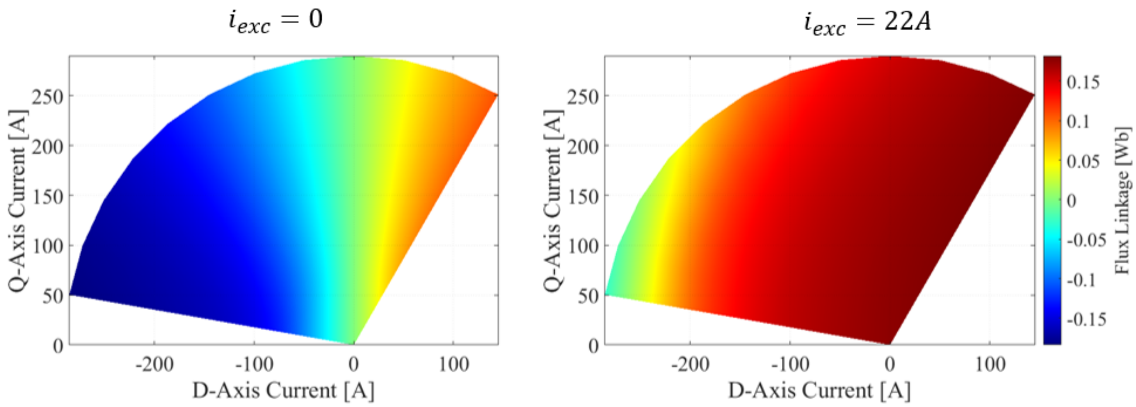

Figure 5.15: D flux linkage map with zero and maximum excitation

d-flux linkage is mainly from the field excitation which is indicated by a high d-flux linkage for almost all values of i_d and i_q while having maximum excitation. The cross-saturation of the stator causes the q-flux linkage in fig 5.16 to decrease as the d-flux linkage increase on account of increased field excitation. Unlike the PMSM, the MTPA line is not shown in fig 5.15 and 5.16. Because, the MTPA points in case of EESM corresponds to different excitation current which means a corresponding flux linkage map for each MTPA point.

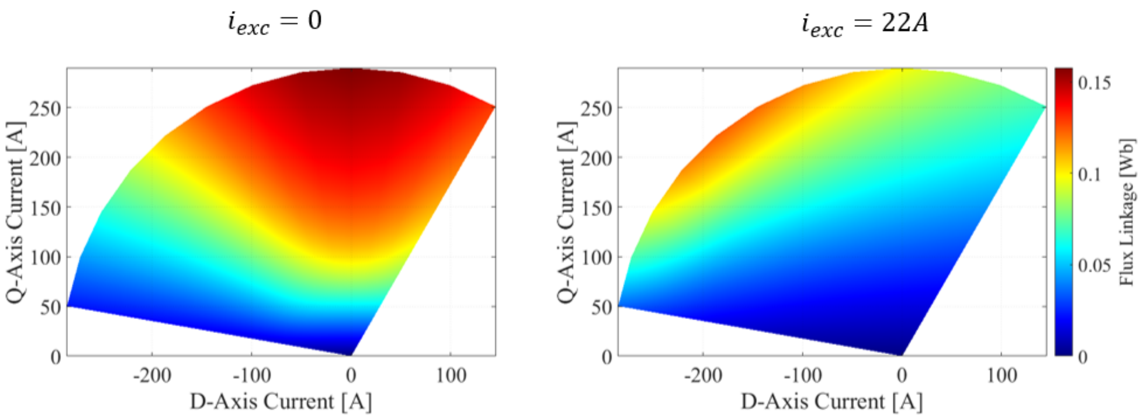

Figure 5.16: Q flux linkage map with zero and maximum excitation

5.4.3 Efficiency map

The efficiency map of the high power machine is calculated similar to the PMSM. However, fewer operating points were considered as the search algorithm takes longer time due to the presence of an additional variable, i_{exc}. The maximum efficiency is is around 91.5%. The base speed of the machine is same as the design speed, 4000 rpm and the peak torque is 198 Nm. The peak torque extends to the design speed of 4000 rpm indicating full utilization of available stator voltage in contrast to high efficiency machine. This confirms with the design intention of producing maximum overloading capablity using the EESM. Comparing to PMSM, the efficiency of EESM is not good at low speed and low torque region because the rotor Cu losses become significant. The power factor is 0.941 at the peak power of 85 kW.

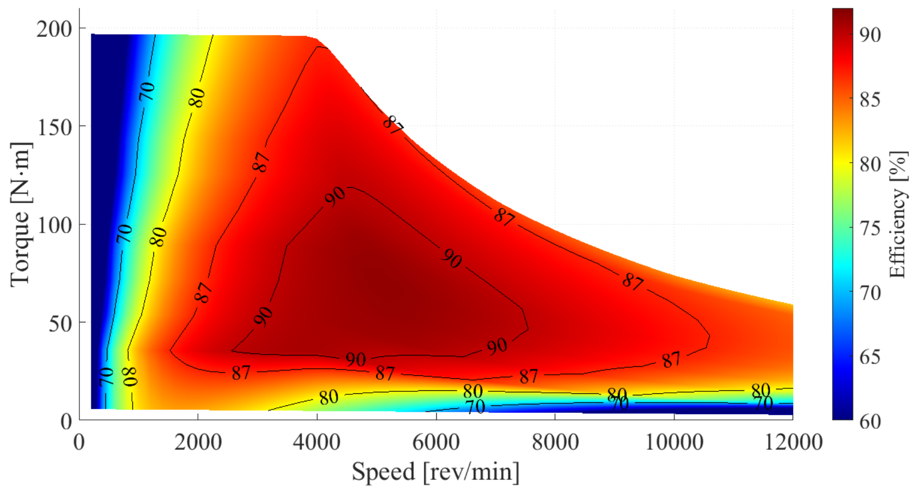

Figure 5.17: Efficiency map of the high power machine

5.5 Design of centralized drive machine

The centralized drive machine was designed with the intent of providing high efficiency as well as sufficient overloading capabilities. Therefore, the stator Cu to iron area ratio, 0.233 is selected to be almost in the middle of high efficiency and high power machine. Similarly, the ratio of rotor to stator outer diameter ratio is selected to be in between the above two machines. The design target was to achieve atleast same peak efficiency as the high efficiency machine with peak power comparable to cumulative of high efficiency and high power machines.

5.5.1 No load performance

As before, the no load performance of the machine is analysed. The no-load flux density distribution is presented in fig 5.18 at $t = 0$. The no-load flux distribution is quite similar to fig 5.6. The rib edges are saturated forcing the flux to pass through the stator teeth and is also confirmed by observing the flux density vector in fig 5.19. The no-load maximum flux density in the stator teeth and yoke of 1.65T and 1.83T respectively is quite similar to the high efficiency machine. The maximum airgap flux density, 1.05T is slightly higher than the high efficiency machine.

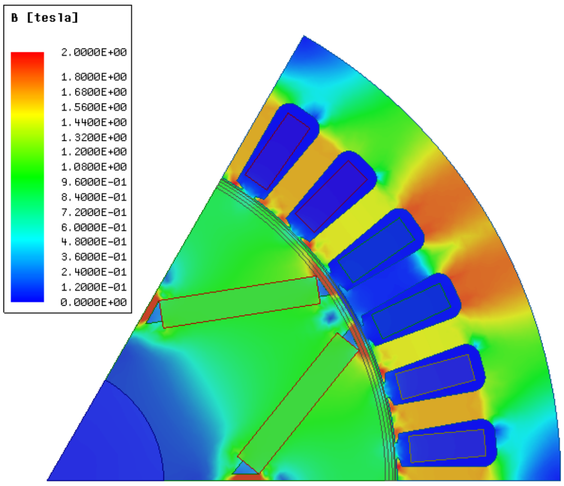

Figure 5.18: Magnetic flux density at no-load and $t = 0$

A very low magnetic flux density close to the shaft in fig 5.6 and 5.18 indicate that the inner portion of the rotor doesn't contribute much to the magnetic circuit in case of PMSM with V-shape rotor geometry. So, a shaft with inferior steel quality or a bigger rotor inner diameter can be used for PMSMs with such magnet geometry without affecting the flux distribution.

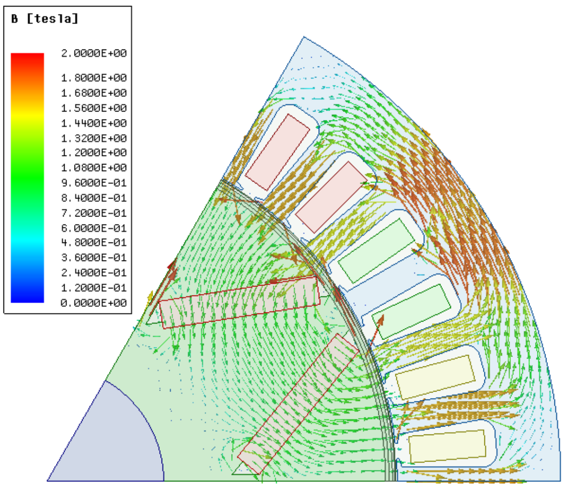

Figure 5.19: Magnetic flux lines at no-load and t=0

The three phase flux linkages and the induced voltages at no load can be observed in fig 5.20. The flux linkage at no-load has almost the same amplitude of 0.148 Wb as the high efficiency machine. Similarly, the flux linkage in phase A is maximum at $t = 0$ confirming the alignment of d-axis with axis of winding phase A. The no load induced voltage at 4000 rpm has a amplitude of 174V which is lightly lower than the high efficiency machine.

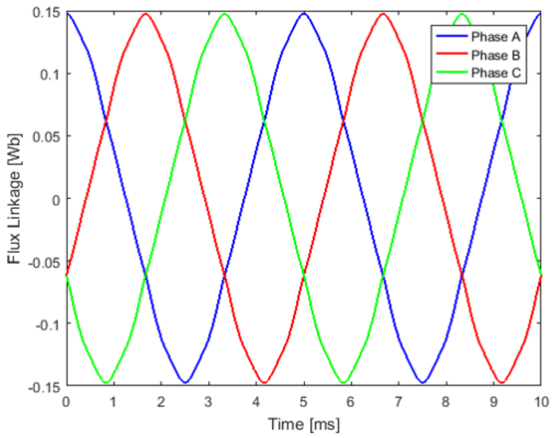

Figure 5.20: Three phase flux linkages and induced voltage at no-load and 4000 rpm

5.5.2 Flux Linkage Map

The d and q flux linkage maps are generated for the centralized drive machine and is presented in fig 5.21 using the same method as for the above two machines. The flux linkage map is very similar to the high efficiency machine which is anticipated as the centralized drive machine is essentially a scaled up version of the high efficiency machine. The MTPA line is also indicated using a black line.

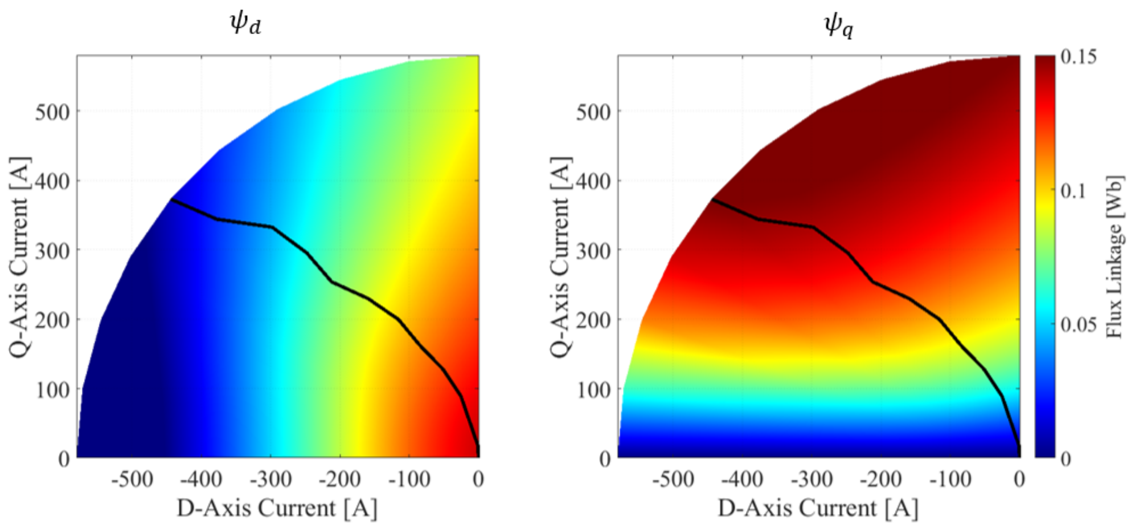

Figure 5.21: D and Q flux linkage maps with MTPA line

5.5.3 Efficiency map

Using the flux linkage maps and methods followed earlier, the efficiency map is generated and is shown in fig 5.22. The efficiency map as expected has similar contours as the high efficiency machine. The peak torque is 318 Nm and extends to 4600 rpm beyond the design speed indicating that higher peak torque may be possible. However, this machine is designed to have both high efficiency and high overloading capabilities and so a compromise is made. The peak efficiency is 96.2% slightly higher than the high efficiency machine. The peak torque is almost equal to the sum of the high efficiency and high power machine. However, the maximum efficiency region occurs during higher torque values compared to the high efficiency machine. The maximum efficiency points occurs where the core and Cu losses are equal. A bigger machine as in this work will usually have higher core losses due to larger iron volume and lower Cu losses for the same torque-speed operating point. Hence, the high efficiency point will tend to move towards the high torque region compared to a similarly designed small machine.

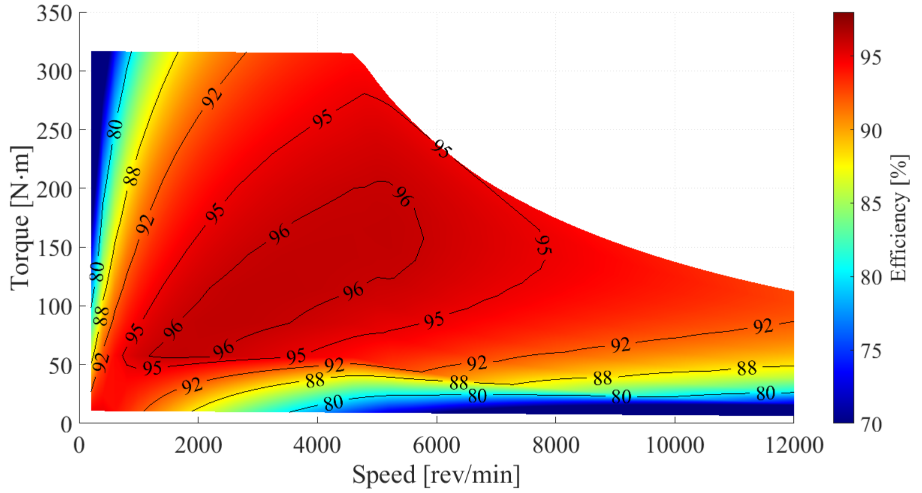

Figure 5.22: Efficiency map of the centralized drive machine

5.6 Drive cycle performance

The efficiency maps of all the three machines were used along with vehicle models and drive cycles to analyse the performance of the machines. The wheel energy along with machine operating efficiency is calculated for each drive cycle and are presented in table 5.6 and 5.7. The absolute value of torque is considered while calculating wheel energy and operating efficiency in this case i.e. it is assumed that the efficiency map of the machine is identical in motoring and generating modes. A gear ratio of 1:10 is used for calculating the machine operating points.

Since, the proposed drive system uses two machines, torque distribution can be used to select the operating points of each of the machine. Three different strategies can be used. First approach can be minimum loss operation of high efficiency machine. It can be used to operate the high efficiency machine at its best operating point and thereby minimizing the cooling requirements of the machine. Second approach is minimum loss operation of high power machine. It can be used if the high power machine doesn't use cooling where the temperature needs to be limited. Third method can be minimum loss in total system including both the machine. In this work, the third approach to maximize the system efficiency is used.

Distributed in table 5.6 and 5.7 corresponds to the proposed drive system using high efficiency and high power machines. There are two cases considered for the distributed drive system. Case 1 assumes that there are no losses in the EESM when not used. It can be possible if a one way clutch is used. In case 2 it is assumed that mechanical losses always occur in the EESM even when not in use. These losses in case 2 are then supplied via the high efficiency machine.

The wheel energy in table 5.6 and 5.7 is quite different for different drive cycles and doesn't necessarily correlate well with the wheel power analysis in table 5.1 and 5.2. Because, the wheel energy not only depends on the power but also on the duration of the drive cycles. Hence, the drive cycle with longer duration usually result in higher wheel energy. It can be observed that for both the type of drive systems the operating efficiency is usually lower than the peak efficiency. It is because most of the drive cycle operating points usually lie in the low torque region as shown in fig 5.23 and the efficiency of both the machine as seen in efficiency maps is lower in these regions with the high efficiency machine being a little better than the centralized drive machine. Fig 5.23 also show that all the drive cycle operating points lie inside the operating boundary for both small and medium car and hence, the drive cycle requirement can be fully satisfied with both drives.

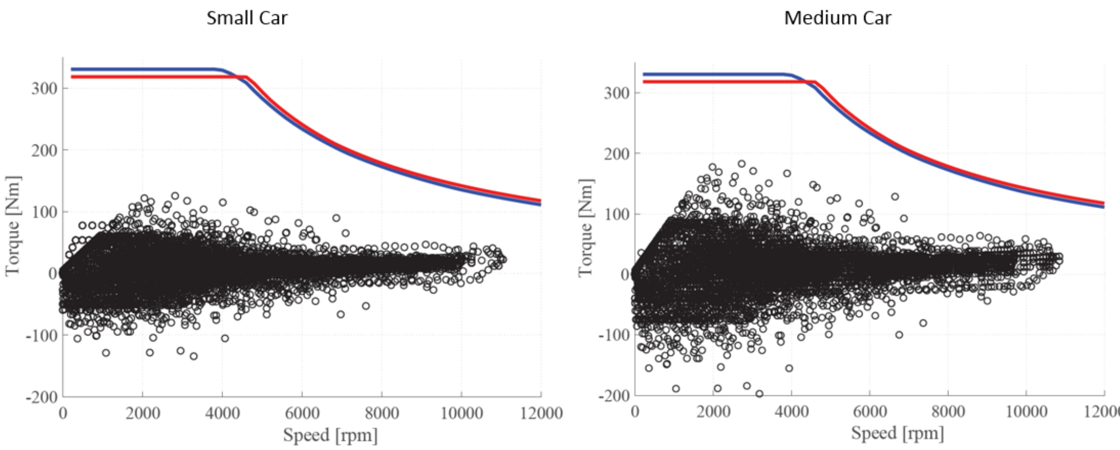

Figure 5.23: Drive cycle operating points of small and medium car with torque speed boundary for distributed and centralized drive

It is evident from table 5.6 and 5.7, the operating efficiency of the centralized drive improves when used with a medium car. The reason might be that the drive cycle operating points for a medium car lies more in the higher efficiency reason indicating that the centralized drive machine design is over-dimensioned for a small car. The operating efficiency varies from 74.02% to 92.72% for a small car and 78.53% to 93.94% for a medium car. The highest operating efficiency of 93.94% is observed in NYCC cycle with a medium car. Similarly, the least efficiency of 74.02% is observed in HWFET drive cycle for a small car. The large variation in operating efficiency is the result of the different operating points for different drive cycles.

Table 5.6: Wheel energy and efficiency analysis of the two drives for a small car

Drive Cycle	Wheel Energy (Wh)	Efficiency (%)		
		Centralized	Distributed	
			Case 1	Case 2
ECE	482.74	87.91	92.26	87.61
NYCC	390	92.72	93.49	92.02
FTP75	2426.68	84.67	90.53	87.01
WLTC Low	438.27	89.56	93.35	90.79
SC03	867.9	85.91	91.08	87.93
WLTC Medium	702.36	86.00	91.43	88.33
JC08	1374.95	85.03	91.25	87.81
EUDC	868.85	78.39	88.22	83.30
UC LA92	2746.34	85.27	90.75	87.42
WLTC High	907.2	79.99	87.70	84.23
HWFET	1664.42	74.02	84.69	80.56
US06	2437.7	81.47	88.36	85.00
WLTC Extra High	1261.29	77.47	85.81	82.64

Table 5.7: Wheel energy and efficiency analysis of the two drives for a medium car

Drive Cycle	Wheel Energy (Wh)	Efficiency (%)		
		Centralized	Distributed	
			Case 1	Case 2
ECE	673.23	90.6	92.94	89.72
NYCC	550.8	93.94	92.62	91.28
FTP75	3314.68	88.22	91.59	87.85
WLTC Low	618.06	92.17	93.76	91.32
SC03	1199.36	89.20	92.07	88.83
WLTC Medium	971.11	89.26	92.71	89.49
JC08	1897.46	88.66	92.78	89.06
EUDC	1123.52	82.66	90.38	84.23
UC LA92	3726.4	88.61	91.62	88.17
WLTC High	1190.9	84.40	89.74	85.12
HWFET	2066.07	78.53	87.36	80.38
US06	3158.95	85.37	89.99	85.79
WLTC Extra High	1558.48	81.69	89.08	82.74

The distributed drive in case 1 results into an overall operating efficiency improvement of around 1% to 10%. This indicates that as the machine becomes smaller, the peak efficiency may decrease but the high efficiency area coincides more with drive cycle operating points. This with the drive cycle operating points in the same region results in high operating efficiency. This is supported by a good operating efficiency range of 85.81% to 93.49% for a small car. Unlike, the centralized drive machine the operating efficiency doesn't improve much in medium car for the same drive cycle. However, the operating efficiency range, 89.08% to 93.94% moves more towards higher efficiency. So, overall an improvement in efficiency is observed. But, in case of case 2, the operating efficiency of the distributed drive is similar compared to centralized drive. This is the result of continuous mechanical losses in the high power machine even when not used.

6
Discussion

The analysis made using the vehicle specification, wheel power and consequently motor design helps in drawing some conclusion towards the suitability of the proposed design as well as confirm certain motivation of the work. There were some aspects that were not considered due to limited scope of the work which form the part of the future work.

6.1 Conclusion

The main conclusion that are drawn from the analysis of the vehicle data, wheel load analysis followed by the design of the three different motors presented in this work can be summarized as follows.

The vehicle specifications of selected BEVs and ICEVs point that most of the BEVs are mainly adapted towards the lower end or base models of the similar ICEVs. The crub weight of the BEVs was found to be a bit higher when compared with the base model of similar ICEVs. Also, the presence of higher end models in case of ICEVs means that superior level of acceleration performance is possible for the same vehicle.

It can be concluded from the wheel power analyses that the peak power requirement of the powertrain is dominated by acceleration performance and varies significantly between different vehicle categories. Also, the fractional loading capability of the electric machines used in the EVs needs to account for the road gradient requirement. Similarly, the continuous rating of the powertrain should consider the loading due to head wind. Contrary to the variation in peak power, the driving power required for constant speed driving on a level road does not vary much between the two car category selected.

It was observed that the similar peak torque could be achieved by distributing the drive. At the same time, the smaller PMSM with a little lower peak efficiency was found to be more suitable for drive cycle operation as the high efficiency region matches with the operating points. It can be concluded that even though higher peak efficiency can be achieved with a bigger machine, the operating efficiency doesn't necessarily be high compared to a smaller one. The proposed drive system resulted in significant efficiency improvements for some drive cycle operation when a one way clutch is used with the high power machine.

6.2 Future work

The analysis carried out in this work helps draw some interesting conclusions. However, it also sheds light into certain aspect that might need to be considered to have a more comprehensive study. These aspects form the part of the future work that are discussed below.

The number of selected ICEVs were lesser than the BEVs. A higher sample size will definitely lead to much obvious pattern in the data. Similarly, the acceleration performance listed by the manufacturer were not considered in this study. The difference in terminology can also be avoided by following a common classification.

The wheel power analysis used a limited number of drive cycles compared to [6]. Additional drive cycles can be used in future to confirm the results. Also, the wheel power analysis can be used to generate operating points of the various drive cycles which then can be studied for different vehicle categories. This can be used to define the design region of the motors in future work.

The motor design was carried out focusing on power and efficiency and other aspects such as torque ripple, thermal calculation and mechanical stress analysis was kept out of the scope. The mechanical stress analysis can actually result in a optimized magnet rib edge thickness and the bridge thickness between magnet ducts. Also, a comparison of different design should be made for each of the machines based on number of poles, number of winding layers, hair pin stator etc.

Finally, the simulations should be supported by experimental measurement. So, prototyping the various machines along with suitable converter design followed by experimental verification can be carried out as part of future work.

6.3 Sustainability and Ethics

BEVs are considered more sustainable mode of transportation compared to their ICEV counterparts. However, to be truly sustainable the energy used to charge the batteries should be from sustainable sources, the materials used in such vehicles should be recyclable or available in abundance and the manufacturing process must also sustainable form of energy to mention a few. So, sustainability of BEVs depends on more of a holistic approach.

In this thesis, the design of electric machine for BEVs is considered. So, the scope of sustainability is considered assuming that the life cycle use of such BEVs is already sustainable from manufacturing to usage by customers. One of the motivation of the work is to improve energy efficiency of BEVs using two different type of machine design. It was observed in the results that such a way of powertrain design have the potential to improve the operating efficiency of the BEVs. This in turn can mean smaller battery pack or less energy usage during vehicle usage cycle. This can be thus considered a more sustainable approach of powertrain design.

However, a PMSM is used as high efficiency machine which uses rare earth materials which may not be considered good from sustainability point of view. It should be kept in mind other applications such as computers, audio systems, wind turbines etc have a higher use stock of such materials compared to automotive. So, new machine design having similar operating point efficiency's along with research in PM recycling or new materials can lead to more sustainable design choices. In future a comparative study will be undertaken by designing an EESM, which does not use rare earth material, as an alternative to PMSM for high efficiency drive.

Bibliography

[1] "The History Of The Electric Car", accessed 2017-02-06. [Online]. Available: https://www.energy.gov/articles/history-electric-car

[2] E. Esmailzadeh , G.R. Vossoughi and A. Goodarzi (2001) "Dynamic Modeling and Analysis of a Four Motorized Wheels Electric Vehicle", Vehicle System Dynamics, 35:3, 163-194. [Online]. Available: http://dx.doi.org/10.1076/vesd.35.3.163.2047

[3] Brown, Stephen, David Pyke, and Paul Steenhof. "Electric vehicles: The role and importance of standards in an emerging market." Energy Policy 38.7 (2010): 3797-3806.

[4] Chen, Xinbo, et al. "An overview of distributed drive electric vehicle chassis integration." Transportation Electrification Asia-Pacific (ITEC Asia-Pacific), 2014 IEEE Conference and Expo. IEEE, 2014.

[5] Liu, Hao, Xinbo Chen, and Xinjian Wang. "Overview and prospects on distributed drive electric vehicles and its energy saving strategy." Prz. Elektrotech 88 (2012): 122-125.

[6] Grunditz, E. "Design and Assessment of Battery Electric Vehicle Powertrain, with Respect to Performance, Energy Consumption and Electric Motor Thermal Capability", ISBN 978-91-7597-412-5, 2016

[7] "Tesla Model S", accessed 2017-02-08. [Online]. Available: https://www.tesla.com/models

[8] "Mercedes SLS AMG Electric", accessed 2017-03-07. [Online]. Available: http://www.mercedes-amg.com/webspecial/sls_e-drive/eng.php

[9] "Siemens VDO announces eCorner motor-in-hub concept", accessed 2017-02-08. [Online]. Available: http://www.autoblog.com/2006/08/10/siemens-vdo-announces-ecorner-motor-in-hub-concept

[10] M. Terashima, T. Ashikaga, T. Mizuno, and K. Natori. "Novel motors and controllers for high-performance electric vehicle with four in wheel motors" , IEEE Trans. Ind. Electron., 1997, 44, 28–38.

[11] Johnston D. "TM4 Motor-Wheel Drive and Control System: Performance, Benefits and Advantages", Proceedings of the 17th International Electric Vehicle Symposium, Montreal, Canada, 2000

[12] Shimizu H, Harada J, Bland C, et al. "Advanced concepts in electric vehicle design[J]. Industrial Electronics" , IEEE Transactions on, 1997, 44(1): 14-18.

[13] Shimizu H K K Y K. “KAZ” The super electric vehicle: Proceedings of the 18th International Electric Vehicle Symposium, Berlin,Germany,2001[C]

[14] Hiroichi Yoshida, Hiroshi Shimizu. Development of high performance electric vehicle “Eliica”. Koyo Engineering Journal English Edition, 2005, 168 (E).

[15] T.D.Gillespie, "Fundamentals of Vehicle Dynamics",1st ed. Society of Automotive Engineers, Inc., 1992

[16] United States Environmental Protection Agency, Vehicle and Fuel Emissions Testing, "Dynamometer Drive Schedules", [Online]. Available: `https://www.epa.gov/vehicle-and-fuel-emissions-testing/dynamometer-drive-schedules`

[17] DieselNet, "Japanese JC08 Cycle", [Online], Available: `https://www.dieselnet.com/standards/cycles/jp_jc08.php`

[18] F. Momen, K. Rahman, Y. Son and P. Savagian, "Electrical propulsion system design of Chevrolet Bolt battery electric vehicle," 2016 IEEE Energy Conversion Congress and Exposition (ECCE), Milwaukee, WI, 2016, pp. 1-8

[19] L. Harnefors, M. Hinkkanen, O. Wallmark and A. G´omez Yepes, "Control of Voltage-Source Converters and Variable-Speed Drives", 2002.

[20] C. Rossi, D. Casadei, A. Pilati and M. Marano, "Wound Rotor Salient Pole Synchronous Machine Drive for Electric Traction," Conference Record of the 2006 IEEE Industry Applications Conference Forty-First IAS Annual Meeting, Tampa, FL, 2006, pp. 1235-1241.

[21] O. Haala, B. Wagner, M. Hofmann, M. Marz, "Optimal Current Control of Externally Excited Synchronous Machines in Automotive Traction Drive Applications", World Academy of Science, Engineering and Technology, International Science Index 81, International Journal of Electrical, Computer, Energetic, Electronic and Communication Engineering, 7(9), 1133 - 1139, 2013

[22] J. S. Hsu, C. W. Ayers, C. L. Coomer, R. H. Wiles, "Report on Toyota/Prius Motor Torque Capability, Torque Property, No-Load Back EMF, and Mechanical Losses", Oak Ridge National Laboratory, 2007

[23] Jato, "Global car market, new car sales, 2016-Q1". [Online]. Available: `http://www.jato.com`

[24] European alternative fuels observatory,"European vehicle category", accessed 2017-04-24, Available: `http://www.eafo.eu/content/european-vehicle-categories`

[25] Du, X. and Graedel, T. E. (2011), Global Rare Earth In-Use Stocks in NdFeB Permanent Magnets. Journal of Industrial Ecology, 15: 836–843. doi:10.1111/j.1530-9290.2011.00362.x

A

Vehicle data

The data for BEVs are obtained from [6] as mentioned earlier. The BEVs are classified in [6] as small, medium-large and sports. In this study only the small and medium-large cars are considered. The data for the selected BEVs are mention in table A.1 and Medium-large BEVs.

The highest selling ICEV models are selected for comparison using [23]. In [23] the ICEVs are classified as A, B, C segments and so on. The same classification is retained. The data of the selected ICEVs are presented in table A.3 - A.6. The data of the selected vehicles are obtained from the broucher of the vehicle models sold in UK market as they are in English and can be assumed to represent the European market. Wherever the data was not unavailable for a particular model, it was obtained from the models sold in US market e.g. Hyrundai Accent, Renault Clio etc. The power is specified in horsepower (hp) and the weight in pounds (lbs) for such models. The following conversion is used to convert to kW and kg respectively.

$$1\,hp = 0.7457\,kW; \qquad 1\,lbs = 0.453592\,kg \tag{A.1}$$

There are many options in case of ICEVs w.r.t. engine peak power, fuel type, transmission type etc. So, it was decided to choose variants with the lowest and highest engine output power and are represented as base and high end models respectively. Hence, the high end model may not be the most expensive. The chosen variant are also mentioned along with vehicle brand and models.

Table A.1: The small BEV vehicle models, curb weight and peak power [6]

Brand and model	Curb weight (kg)	Peak Power (kW)
Smart Fortwo	900	55
Smart BRABUS	1000	60
Toyota iQ EV	1100	47
Fiat 500e	1355	83
Citroen C-ZERO	1120	49
Peugeot iOn	1120	47
Mitsubishi i-MiEV	1085	49
Volkswagen e-up!	1139	60
Chevrolet Spark EV	1300	60
Bollore Bluecar	1120	50
Mitsubishi MiniCab	1110	30

Table A.2: The medium-large BEV vehicle models, curb weight and peak power [6]

Brand and model	Curb weight (kg)	Peak Power (kW)
BMW i3	1195	125
Renault Zoe	1468	65
Volvo C30 El	1725	89
Volkswagen e-Golf	1510	85
Nissan Leaf	1516	80
Honda FIT EV	1475	92
Renault Fluence Z.E.	1535	70
Ford	1642	107
Kia Soul El	1490	81.4
Mercedes-Benz B-Class El.Dr.	1650	132
BYD e6	2380	90
Nissan e-NV200(Evalia)	1571	80
Toyota RAV4 EV	1828	115

Table A.3: Vehicle model, variant, peak power and curb weight data of ICEVs (B segment base models)

Brand and model	Variant	Curb weight (kg)	Peak Power (kW)
Volkswagen Polo	S, S A/C 1l 60 PS	1055	44
Ford Fiesta	1.25 Duratech (60 PS)	1044	44
Toyota Yaris	1l VVT-i 5-speed M	975	51
Kia Rio	1.25 83bhp	1127	83hp
Renault Clio	Expression 1.2 16V 75	1059	54
Peugeot 208	1.2l PureTech 68	960	50
Opel Corsa	1.4i (75PS) ecoFLEX	1000	55
Hyundai Accent	SE Hatchback	2489lbs	137hp

Table A.4: Vehicle model, variant, peak power and curb weight data of ICEVs (B segment high models)

Brand and model	Variant	Curb weight (kg)	Peak Power (kW)
Volkswagen Polo	GTI TSI 192 S	1280	141
Ford Fiesta	1.6 EcoBoost (182 PS)	1163	134
Toyota Yaris	1.33l Dual VVT-i A	1160	73
Kia Rio	1.4 107bhp ISG	1236	107hp
Renault Clio	1.6 Turbo R.S. 220 Trophy	1204	162
Peugeot 208	1.6l THP 208 S&S GTi	1160	153
Opel Corsa	1.4i Turbo (150PS) Start/Stop	1200	110

Table A.5: Vehicle model, variant, peak power and curb weight data of ICEVs (C segment base models)

Brand and model	Variants	Curb weight (kg)	Peak Power (kW)
Toyota Corolla	1.33l Dual VVT-i Petrol G M/T	1150	73
Volkswagen Golf	S 1.2l TSI 85 PS	1205	63
Ford Focus	5 door 1.6 Ti-VCT (85 PS)	1264	63
Hyundai Elantra	1.6 MPi Gasoline Manual FWD	1250	127.5hp
Volkswagen Jetta	S, SE 2.0l Bluemotion Technology	1395	81
Hyundai Civic Sedan	LX 110PS,CVT	2742lbs	158hp
Chevrolet Cruze	L Manual 2016	2835lbs	153hp

Table A.6: Vehicle model, variant, peak power and curb weight data of ICEVs (C segment high models)

Brand and model	Variants	Curb weight (kg)	Peak Power (kW)
Toyota Corolla	1.6l Valvematic Petrol M/D S	1325	97
Volkswagen Golf	R 2.0l TSI 300 PS 4 motion	1476	221
Ford Focus	Estate 2.0 Ecoboost 250 PS Start/Stop	1386	184
Hyundai Elantra	2.0 MPi Gasoline	2857lbs	152hp
Volkswagen Jetta	GT 2.0l TDI 150PS Bluemotion	1448	110
Hyundai Civic Sedan	Touring	2923lbs	174hp
Chevrolet Cruze	LS Manual	2835lbs	153hp

B
Machine data

In this work, three machines were designed as explained earlier. Some of the dimensional detail is already included previously in chapter 4. The detailed specifications of the three machines are presented in table B.1.

Table B.1: The specifications of the three machines designed in the work

	High efficiency	High power	Centralized
Peak power (kW)	61	85	140
Peak torque (Nm)	133	197	318
Base speed (rpm)	4600	4000	4600
Apparent power (kVA)	81	90	176
Max stator Jrms (A/mm^2)	18	30	18
Max rms phase current (A)	178	282	410
Peak efficiency (%)	95.8	90.2	96.2
Stack length (mm)	100	100	125
Number of turns	7	6	4
Number of strands	4	3	4
Wire diameter (mm)	0.912	0.861	0.965
Stator outer diameter (mm)	175	175	220
Stator inner diameter (mm)	116	121	150
Tooth width (mm)	4.4	6	6.2
Tooth height (mm)	17.1	12.3	18.5
Slot opening width (mm)	2.65	2	3.2
Slot area (mm^2)	139.77	79.44	178.11
Rotor outer diameter (mm)	114.4	119	150
Shaft diameter (mm)	40	40	50
Airgap (mm)	0.8	1	1
Magnet width (mm)	53		68
Magnet thickness (mm)	4.8		5.97

The material used for the core, SURA M250-35A is same for all the machines. It is also used in the shaft even though in reality inferior materials can be used. The core stacking factor for all three machine is 0.95. Stranded round conductors are used and the details are mentioned in table B.1. Whole coil arrangement is used for the stator coils of all three machines. The slot area shown in table B.1 is obtained from RMxpert. The magnet material used in the PMSM is NdFeB which is also used in [6]. The max MMF of the high power machine is 2970 Aturns.